

Non-linear saturation of gravito-inertial modes excited by tidal resonances in binary neutron stars

Alexis Reboul-Salze¹, Aurélie Astoul², Hao-Jui Kuan¹, Arthur G. Suvorov^{3,4}

¹ Max Planck Institute for Gravitational Physics (Albert Einstein Institute), D-14476 Potsdam, Germany
e-mail: alexis.reboul-salze@aei.mpg.de

² School of Mathematics, University of Leeds, Leeds LS2 9JT, UK

³ Departament de Física Aplicada, Universitat d'Alacant, Ap. Correus 99, E-03080 Alacant, Spain

⁴ Theoretical Astrophysics, IAAT, University of Tübingen, Tübingen, D-72076, Germany

Received ??; ??

ABSTRACT

Context. During the last seconds of a binary neutron-star merger, the tidal force can excite stellar oscillation modes to large amplitudes. From the perspective of premerger electromagnetic emissions and next-generation gravitational-wave detectors, gravity (g -) modes constitute a propitious class. However, existing estimates for their impact employ linear schemes which may be inaccurate for large amplitudes, as achieved by tidal resonances. With rotation, inertial modes can be excited as well and while their non-linear saturation has been studied, an extension to fully-consistent gravito-inertial modes, especially in the neutron-star context, is an open problem.

Aims. We study the linear and non-linear saturation of gravito-inertial modes and investigate the astrophysical consequences for binary neutron-star mergers, including the possibility of resonance-induced dynamo activity.

Methods. A new (non-)linear formulation based on the separation of equilibrium and dynamical tides is developed. Implementing this into the 3D pseudo-spectral code MagIC, a suite of non-linear simulations of tidally-excited flows with an entropy/composition gradient in a stably-stratified Boussinesq spherical-shell are carried out.

Results. The new formulation accurately reproduces results of linear calculations for gravito-inertial modes with a free surface for low frequencies. For a constant-density cavity, we show that the axisymmetric differential rotation induced by nonlinear ${}_2g$ and ${}_1g$ modes may theoretically be large enough to amplify an ambient magnetic field to $\gtrsim 10^{14}$ G. In addition, rich non-linear dynamics are observed in the form of a parametric instability for the ${}_1g$ mode. The stars are also spun-up, which extends the resonance window for any given mode.

Conclusions. This study provides non-linear numerical support for a recently-proposed scenario where, to accommodate the non-thermal precursor flares seen in some short gamma-ray bursts, the magnetic field of a premerger star is amplified by resonant g -modes. It further suggests that g -mode resonances may have a stronger impact on gravitational-wave signals than previously estimated.

Key words. Tidal interaction – Stars: neutron – binaries: general – hydrodynamics – waves – methods: numerical

1. Introduction

Binaries are common in Nature, with some estimates of stellar multiplicity being close to unity based on modern astrometric surveys (Duchêne & Kraus 2013; El-Badry 2024). Tidal forces play an important role in the rotational and orbital evolution of close systems, such as binary stars (e.g. Zahn 2013; Barker 2022, and references therein), exoplanetary hot-Jupiter systems (e.g. Jackson et al. 2008; Bolmont & Mathis 2016; Lazovik et al. 2024), planet-satellite systems (Counselman 1973; Fuller et al. 2024, for a review), and merging neutron stars (NSs; Damour & Nagar 2009; Taniguchi & Shibata 2010). Their impact can generally be quantified in terms of two components, being the equilibrium and dynamical tides. The former exist even in the zero-frequency limit and describe bulk geometric large-scale deformations, while the latter relate to the excitation of internal (damped) waves (e.g. Ogilvie 2014; Hinderer et al. 2016; Andersson & Pnigouras 2020).

A perturbative, and often even linear, treatment of tides provides an excellent approximation in many astrophysical systems of interest. There are cases however where the validity of a linear scheme is less certain (see section 4 of Ogilvie 2014, for a review). One such scenario – central to this paper – in-

volves resonances in NS mergers. As the binary compactifies due to gravitational-wave (GW) radiation-reaction, the orbital frequency ‘chirps’ upwards towards coalescence (e.g. Peters 1964). When the tidal driving frequency approaches the oscillation frequency of a mode inside one of the stars, that mode’s amplitude grows rapidly until saturating at a value that depends on the degree of orthogonality between its eigenfunction and the appropriate multipole component of the tidal field (‘overlap’; Press & Teukolsky 1977; Alexander 1987). For some mode classes, the saturation amplitude could theoretically reach fractions of unity where non-linear corrections need to be taken into account to more accurately assess how tides affect GW or electromagnetic observables; see Suvorov et al. (2024a) for a recent review.

Numerical relativity simulations have highlighted the impact of non-linearities on GW dephasing for the fundamental (f -) mode (Kuan et al. 2024). Though subdominant, gravity (g -) modes, supported by internal composition and/or entropy gradients, may also non-negligibly accelerate inspiral in mergers as their eigenfrequencies are sufficiently low ($\sim 10^2$ Hz) that they can be excited \sim seconds prior to coalescence while maintaining sizeable overlaps (Kokkotas & Schafer 1995; Kuan et al. 2021a; Passamonti et al. 2021; Hegade K. R. et al. 2024). Since these

modes offer valuable microphysical information and it is hoped that templates will be matched to GW data in the future, it is important that their non-linear saturation be quantified. For stars retaining a high angular frequency into old age ($\Omega \gtrsim 10^2$ Hz; ‘recycled pulsars’) the inertial class of modes (restored by Coriolis acceleration) may also be relevant (Lai & Wu 2006; Suvorov & Kokkotas 2020). With both buoyancy and rotation present, the two branches merge to some degree and go under a ‘gravito-inertial’ label (see, e.g., Aerts & Tkachenko 2024). Here we present a method to model the non-linear saturation of such hybrid modes. Note in particular that nonlinearities are treated at the level of the magnetohydrodynamic (MHD) equations of motion, rather than via secondary couplings between linear modes as studied previously (e.g. Weinberg et al. 2013; Pnigouras & Kokkotas 2015; Zhou & Zhang 2017). This marks the first time therefore that this class and their saturation have been modeled consistently at a non-linear level for rotating, tidally-forced NSs.

Non-linear, tidally-forced inertial modes have been studied in numerical simulations modeling convective envelopes of giant gaseous planets and low-mass stars in close binaries systems (Favier et al. 2014; Barker 2016; Astoul & Barker 2022). Due to the generation of differential rotation, transfer rates of tidal energy (i.e. tidal dissipation) can be either larger or smaller by up to ~ 3 orders of magnitude relative to linear-theory predictions at some frequencies (especially for thin shells, high tidal amplitudes, and low viscosities; Astoul & Barker 2023). In radiative regions, differential rotation can also arise from the deposition of gravity wave angular momentum at corotation resonances – when the phase velocity of the wave matches the local speed of the fluid – as predicted by Goldreich & Nicholson (1989) in early-type stars envelopes. This result has been confirmed for the radiative cores of solar-like stars in 2D and 3D spherical nonlinear simulations, where the core is progressively spun up from inside out by tidal gravity wave breaking (or weakly non-linear damping) near the center of the star (Barker & Ogilvie 2010; Barker 2011; Guo et al. 2023). Here, we also study such non-linear effects but in the context of gravito-inertial modes in NSs by building on the formulation used in Astoul & Barker (2023) to split tides into equilibrium and dynamical components while adding buoyancy and thermal diffusion.

Based on this ‘split formulation’, accounting for the fact that the Brunt-Väisälä (BV) frequency of a cold NS is typically much smaller than its dynamical (hydrostatic) response frequency, we use the pseudo-spectral MagIC¹ code (Wicht 2002; Gastine & Wicht 2012; Schaeffer 2013) to solve the hydrodynamical equations in a spherical shell under the Boussinesq approximation (Spiegel & Veronis 1960). The equations are coupled to the leading-order ($\ell = m = 2$) tidal potential for frequencies relevant to the late-stages of inspiral, with (effective) viscosity included in anticipation of damping and turbulence. Magnetic effects may be especially relevant in some mergers, as there is evidence to suggest that those systems which release nonthermal gamma-ray burst (GRB) precursor flares ($\lesssim 5\%$ of mergers; Wang et al. 2020; Coppin et al. 2020) contain magnetars with near-surface fields of $B \gtrsim 10^{13}$ G (e.g. Xiao et al. 2024). Fields of this strength can influence mode spectra (e.g. Suvorov et al. 2022; Kuan et al. 2021a) or merger dynamics directly (e.g. Ciolfi 2020). A thorough comparison with a linear scheme, using the DedaLus3 code (Burns et al. 2020), is also provided to explore the direct impact of non-linearities.

Although this is primarily a ‘methods’ paper where the above-described strategy is presented in detail and then inte-

grated numerically for a variety of setups, we also explore some astrophysical applications. For example, incorporating magnetic fields naturally allows for the investigation of dynamo action, namely the magnetorotational instability (MRI; Balbus & Hawley 1998; Astoul & Barker 2025), sourced by the differential rotation induced by non-axisymmetric mode activity. The non-linear scheme allows, in principle, for us to compare with the idea suggested by Suvorov et al. (2024b) that magnetar-level fields are generated on the verge of coalescence rather than preserved over cosmological timescales, as such longevity appears difficult to reconcile with magnetothermal evolutions (Pons & Viganò 2019).

This paper is organized as follows. Sec. 2 introduces the neutron-star hybrid modes and the equations governing both the linear (Sec. 2.2.1) and new non-linear (Sec. 2.2.2) schemes used throughout, with details on numerical implementation provided in Sec. 2.4. Results for both g - and more general gravito-inertial modes in cases with rotation are given in Sec. 3 for the linear and Sec. 4 for the non-linear cases, respectively. Astrophysical implications are briefly explored in Sec. 5, with discussion provided in Sec. 6. Key results are summarized in Sec. 7.

2. Modeling of the tidal resonance of gravito-inertial in a neutron star binary

2.1. Simplified neutron star model

In this article, we study the tidal forcing of gravito-inertial modes in the late stages of a binary neutron-star inspiral. To do this, we use methods and formulations from the stellar and planetary community, where linear codes and more recently non-linear simulations are developed following the split methodology mentioned earlier. As a first study in the context of binary neutron stars, we adopt the idealized Boussinesq approximation that allows us to study the impact of stable entropy/composition stratification while keeping the simulations computationally efficient so that the parameter space can be efficiently explored. This approximation corresponds to assuming that variations in mass density can be neglected except as they contribute to buoyancy, i.e., the fluid is otherwise incompressible and soundwaves are filtered (Spiegel & Veronis 1960). This approximation is justified because the velocities of resonant modes, as found in previous studies (Kuan et al. 2021a; Passamonti et al. 2021; Suvorov et al. 2024b), are strictly subsonic. We use the Newtonian Navier-Stokes equations throughout and neglect the effects of general relativity, as the Boussinesq approximation is already a more restrictive approximation. Note that we also assume the neutron-star interior to contain only a normal fluid, ignoring superfluidity and superconductivity.

The fluid stratification is characterized by the BV frequency,

$$N^2 \equiv -\frac{g}{\rho_0} \left(\frac{\partial \rho}{\partial S} \Big|_{\rho, Y_e} \frac{dS}{dr} + \frac{\partial \rho}{\partial Y_e} \Big|_{\rho, S} \frac{dY_e}{dr} \right), \quad (1)$$

where g , ρ_0 , ρ , S , P and Y_e are, respectively, the gravitational acceleration, uniform density (see below), density, entropy, pressure, and electron fraction. As a simplification, we assume that the BV frequency depends only on one dimensionless buoyancy variable, chosen here as $b = -\frac{\rho}{\rho_0}$. In this work, we refer to the diffusion process associated with this buoyancy variable as the thermal diffusivity, κ_{th} . This does not reduce the (numerical) generality of the problem as the buoyancy variable could be entropy or composition and would play exactly the same role. For dissipation processes, we adopt uniform profiles of viscosity ν and

¹ <https://magic-sph.github.io>

thermal κ_{th} (or compositional κ_{comp}) diffusivities with $\nu = \kappa_{th}$ for the sake of simplicity².

The model for the NS we use is that of a spherical shell with a uniform density ρ_0 . The latter quantity is determined by the mass of the primary, given as $M_1 = \frac{4}{3}\pi\rho_0 R_o^3$, where R_o is the stellar radius of the primary and depends on the equation of state (EOS). To avoid modeling the stellar core, due to both sizable uncertainties (which only increase during evolution) in microphysical inputs we require and numerical stability reasons, we suppose the shell has an inner radius R_i whose ratio to the stellar radius (R_o) is set as $\alpha \equiv \frac{R_i}{R_o} = 0.5$. This value has been used in previous studies for planets and stars as a standard (e.g. Favier et al. 2014; Astoul & Barker 2022; Pontin et al. 2023). For astrophysical applications to NSs, we take instead $\alpha = 0.1$ to approximate a whole NS without increasing numerical costs (see Sec. 5.2.2).

2.2. Governing equations

We place ourselves in a frame rotating with the star and assume an initial hydrostatic balance, i.e. $\rho_0 g = -\frac{d\tilde{P}}{dr}$ where g is the gravitational acceleration and \tilde{P} is the background pressure. The equations for the perturbed velocity components can then be written as

$$\nabla \cdot \mathbf{u} = 0, \quad (2)$$

$$\frac{\partial \mathbf{u}}{\partial t} + (\mathbf{u} \cdot \nabla)\mathbf{u} = -\frac{\nabla p}{\rho_0} - 2\boldsymbol{\Omega}_s \times \mathbf{u} - b\mathbf{g} - \nabla\Psi + \nabla \cdot \boldsymbol{\tau}_v, \quad (3)$$

where \mathbf{u} , p and b are velocity, pressure and buoyancy perturbations, $\boldsymbol{\Omega}_s$ is the (constant) stellar angular frequency of the background star, Ψ is the tidal potential, and $\boldsymbol{\tau}_v$ is the viscous stress tensor. Note that the components of velocity are designated by u_i with $i \in [r, \theta, \phi]$ instead of the contravariant equivalent (u^i) in GR calculations. Centrifugal and other forces which may lead to a non-spherical cavity are neglected. We choose to neglect perturbations to the gravitational potential for the sake of simplicity and because they are expected to be quantitatively small in the context of our Boussinesq system (Ogilvie & Lin 2004). This hypothesis is discussed in detail in Sec. 6.4. This makes it easier to compare between formulations as we will neglect the contributions of the gravitational potential perturbations due to the equilibrium tides characterized by the Love number k_2 (See Sec. 6.4).

The heat equation thus takes the form

$$\frac{\partial b}{\partial t} + (\mathbf{u} \cdot \nabla)b + u_r \frac{d\tilde{b}}{dr} = \kappa_{th} \nabla^2 b, \quad (4)$$

where the global gradient of the buoyancy variable $\frac{d\tilde{b}}{dr}$ is linked to the radially dependent BV frequency through

$$N^2 = -\frac{g}{\rho_0} \frac{d\tilde{b}}{dr}. \quad (5)$$

In the case of entropy or composition stratification, we would have $\frac{d\tilde{b}}{dr} = \frac{\partial \rho}{\partial S} \Big|_{P, Y_e} \frac{dS}{dr}$ or $\frac{d\tilde{b}}{dr} = \frac{\partial \rho}{\partial Y_e} \Big|_{P, S} \frac{dY_e}{dr}$, respectively.

Leaving aside events involving dynamical capture, orbital eccentricity is expected to be erased long before coalescence in a neutron-star binary merger (e.g. Peters 1964). Because of

² Note that a realistic estimate of the compositional Prandtl number for mature NSs can be found in Suvorov et al. (2024b), viz. $Pr \equiv \nu/\kappa_{comp} \sim 10^3 - 10^8$. The influence of Pr on mode dynamics is left to future studies.

this, we consider a circular but asynchronous orbit with no spin-orbit misalignment (though cf. Kuan et al. 2023). The dominant (quadrupolar) component of the tidal potential can be written as (e.g. Zahn 1966)

$$\Psi = \Psi_0 r^2 Y_2^2(\theta, \phi) e^{-i\hat{\omega}t}, \quad (6)$$

where Y_ℓ^m is a spherical harmonic of degree ℓ and order m , and the strength of the potential is (see, for instance, equation 3 and table 1 in Ogilvie 2014)

$$\Psi_0 = \sqrt{\frac{6\pi}{5}} \frac{M_2}{M_1} \omega_d^2 \left(\frac{R_o}{a}\right)^3, \quad (7)$$

where M_2 is the companion mass, a is the orbital semi-major axis, and $\omega_d = \sqrt{GM_1/R_o^3}$ is the dynamical frequency with G being the gravitational constant. In the rotating frame introduced earlier, the tidal forcing frequency reads $\hat{\omega} = 2(\Omega_o - \Omega_s)$, where Ω_o is the orbital frequency, and we note that $\hat{\omega}$ can be negative. Equations (2)–(4) constitute the full non-linear equations considered here.

2.2.1. Linear equations

To have a point of comparison with previous literature we first derive the equations describing linear gravito-inertial modes. These are similar to those from Pontin et al. (2024), which read

$$\nabla \cdot \mathbf{u} = 0, \quad (8)$$

$$\frac{\partial \mathbf{u}}{\partial t} = -\frac{\nabla p}{\rho_0} - 2\boldsymbol{\Omega}_s \times \mathbf{u} - b\mathbf{g} - \nabla\Psi + \nu \nabla^2 \mathbf{u}, \quad (9)$$

$$\frac{\partial b}{\partial t} + u_r \frac{d\tilde{b}}{dr} = \kappa_{th} \nabla^2 b. \quad (10)$$

In this study, we consider three distinct BV profiles: a uniform BV frequency in Sec. 3, a uniform buoyancy variable gradient, which leads to a BV frequency varying radially and linearly with the gravitational acceleration of a homogeneous body, $\mathbf{g} = -g\mathbf{e}_r = -g_0 r \mathbf{e}_r$ in Sec. 4, and a realistic profile from Suvorov et al. (2024b) in Sec. 5. To solve the linear system, we take a non-penetrating boundary condition for the radial velocity at the inner boundary and a free surface where normal stress vanishes at the outer boundary following Pontin et al. (2023, 2024). We further impose stress-free conditions (no tangential stress) at both boundaries, with fixed buoyancy variable ($b = 0$) or its gradient ($\frac{\partial b}{\partial r} = 0$) at both boundaries as it plays little impact on the resonances (Pontin et al. 2023). This setup will be referred to as a ‘‘full formulation’’ hereafter as it encompasses both the equilibrium and dynamical tides. However, the implementation of a free surface in a fully non-linear code is both prohibitively costly as surface oscillations would occur at frequencies of $\sim \omega_d$, while the rotation rate and (gravito-inertial or BV frequency) mode frequencies are much lower for NSs.

2.2.2. A new formulation to excite gravito-inertial modes

A derivation for separating equilibrium and dynamical tides, especially for inertial modes, can be found in numerous studies (see, for example, Ogilvie & Lin 2004; Zahn 2013; Ogilvie 2013; Astoul & Barker 2022, and references therein). For the treatment of the gravito-inertial modes, we take a slightly different approach as the one used in Dhoubib et al. (2024): as the equilibrium tide corresponds to the instantaneous hydrostatic response to the tidal force, we assume that reequilibration between pressure and

gravity is reached instantaneously compared to the buoyancy variables (i.e., b in the current context). Another way of describing this treatment is to assume that the advection of the background gradient of the buoyancy variables by the equilibrium tide is part of the heat equation (4) for the dynamical tides. Then the heat equation for the equilibrium buoyancy variable (i.e. b_e) would be

$$\frac{\partial b_e}{\partial t} = \kappa_{th} \nabla^2 b_e, \quad (11)$$

which gives $b_e = 0$ as there are no sources terms. This corresponds to assuming that the equilibrium tide flow \mathbf{u}_e is fully incompressible, and thus we adopt the expression valid for $\ell = m = 2$ inertial modes (Ogilvie 2013; Lin & Ogilvie 2018; Astoul & Barker 2022, 2023)

$$\mathbf{u}_e = \text{Re}[i\hat{\omega} \nabla X e^{-i\hat{\omega}t}] \quad (12)$$

with

$$X(r, \theta, \phi) = \frac{C_t}{2(1 - \alpha^5)} \left[r^2 + \frac{2}{3} \alpha^5 r^{-3} \right] Y_2^2(\theta, \phi), \quad (13)$$

where \mathbf{u}_e is satisfying the free-surface boundary condition at the top and impenetrability at the bottom. Here $C_t = (1 + \text{Re}[k_2^2]) \epsilon$ is the tidal force amplitude related to the real part of the quadrupolar Love number $\text{Re}[k_2^2]$ and the tidal amplitude parameter $\epsilon = (M_2/M_1) (R_o/a)^3$.

Equation (12) leads to a static pressure perturbation p_e that, in addition to \mathbf{u}_e , compensates the tidal force in the Navier-Stokes equations. With this equilibrium tide, the linear equations for the leftover velocity $\mathbf{u}' = \mathbf{u} - \mathbf{u}_e$, pressure $p' = p - p_e$ and $b' = b - b_e$ become

$$\nabla \cdot \mathbf{u}' = 0, \quad (14)$$

$$\frac{\partial \mathbf{u}'}{\partial t} = -\frac{\nabla p'}{\rho_0} - 2\mathbf{\Omega}_s \times \mathbf{u}' - 2\mathbf{\Omega}_s \times \mathbf{u}_e - s\mathbf{g} + \nu \nabla^2 \mathbf{u}', \quad (15)$$

$$\frac{\partial b'}{\partial t} + u'_r \frac{db'}{dr} = -u_{e,r} \frac{db'}{dr} + \kappa_{th} \nabla^2 b'. \quad (16)$$

This system has two effective tidal forcing: $\mathbf{f}_t = -2\mathbf{\Omega}_s \times \mathbf{u}_e$, the Coriolis acceleration on the equilibrium tidal flow \mathbf{u}_e in the momentum equation, and $\mathbf{f}_N = -\mathbf{u}_e \cdot \nabla \tilde{b}$, the advection of the background entropy gradient by the equilibrium tide in the heat equation. This second term will allow us to excite g-modes even in a non-rotating case. It is usually not included in more general split formulations, where background density is not uniform (Ogilvie & Lin 2004; Dhoubit et al. 2024), as it is considered as part of a equilibrium tidal buoyancy variable (i.e., entropy/temperature) term. This approach may lead to issues for g-modes in a uniform density star that may not be present with a non-uniform density, depending on the definition of the equilibrium tide. Indeed, in the Boussinesq approximation, we consider that density perturbations are only due to entropy/composition perturbations but, as described by Ogilvie (2014), such a density perturbation corresponds to a delta spike at the surface with radial displacement. The heat equation would then force the radial displacement to be zero, yielding a contradiction. Our formalism is a workaround to avoid this issue. A comparison between formalisms with a non-uniform density ρ_0 is planned in a further study. The use of a fixed surface also means we cannot have surface modes and, therefore, our formalism is valid for $\Omega_s^2, N^2 \ll \omega_d^2$, which is the case for NSs and main-sequence stars (Ogilvie 2013; Suvorov et al. 2024b).

In the following, we omit primes when using the above-introduced formulation, hereafter called the "split formulation", where the non-linear equations read

$$\nabla \cdot \mathbf{u} = 0, \quad (17)$$

$$\frac{\partial \mathbf{u}}{\partial t} + (\mathbf{u} \cdot \nabla) \mathbf{u} = -\frac{\nabla p}{\rho_0} - 2\mathbf{\Omega}_s \times \mathbf{u} + \mathbf{f}_t - b\mathbf{g} + \nabla \cdot \boldsymbol{\tau}_\nu, \quad (18)$$

$$\frac{\partial b}{\partial t} + (\mathbf{u} \cdot \nabla) b + u_r \frac{db}{dr} = -u_{e,r} \frac{db}{dr} + \kappa_{th} \nabla^2 b. \quad (19)$$

With this split formulation, we use non-penetrating boundary conditions for the velocity at both outer and inner boundaries. We also keep the stress-free boundary conditions as in the previous formulations. For both formulations, we tested that the buoyancy variable boundary conditions did not impact significantly the results and choose therefore the one that gave the strongest amplitude: setting the gradient of the buoyancy variable to zero, i.e. $\frac{db}{dr} = 0$.

2.2.3. Energy equations

As we have a new forcing term in the equations, we focus on deriving the new energy balance to understand the dissipation and saturation of tidally-forced modes. The dissipation terms correspond to the volume integrated viscous D_ν and thermal D_κ dissipation rates given by

$$D_\nu = -\int_V \rho_0 \nu \mathbf{u} \cdot \nabla^2 \mathbf{u} \, dV, \quad D_\kappa = -\int_V \rho_0 \kappa_{th} \frac{g^2}{N^2} b \nabla^2 b \, dV. \quad (20)$$

By the standard definition of work, the power injected by the tidal force in the full formulation is

$$P_\Psi = \int_V \rho_0 \mathbf{u} \cdot (-\nabla \Psi) \, dV. \quad (21)$$

In this formulation, the energy balance has already been derived by Pontin et al. (2023, 2024) and is given by

$$P_\Psi = \frac{dE_K}{dt} + \frac{dE_{PE}}{dt} + D_\nu + D_\kappa, \quad (22)$$

where E_K and E_{PE} are, respectively, the kinetic and potential energy of the star. Their respective rates of change are

$$\frac{dE_K}{dt} = \int_V \frac{\rho_0}{2} \frac{\partial |u|^2}{\partial t} \, dV, \quad \frac{dE_{PE}}{dt} = \int_V \frac{g^2}{2N^2} \frac{\partial b^2}{\partial t} \, dV, \quad (23)$$

except for $N^2 = 0$ where one has $\frac{dE_{PE}}{dt} = 0$. At saturation and averaged over a forcing period of $2\pi/\hat{\omega}$, energy conservation implies

$$P_\Psi = D_\nu + D_\kappa. \quad (24)$$

For the split formulation, the power injected by the effective body force \mathbf{f}_t due to Coriolis force of the equilibrium tide is given by

$$P_{Cor} = \int_V \rho_0 \mathbf{u} \cdot \mathbf{f}_t \, dV. \quad (25)$$

To obtain the power for the effective forcing \mathbf{f}_N in the heat equation, it is easier to use the buoyancy power in the Navier-Stokes equation that is defined by

$$P_{buoy} = -\int_V \rho_0 u_r b g \, dV. \quad (26)$$

By substituting u_r using the heat equation, we obtain the buoyancy power due to the tidal entropy forcing

$$P_{buoy,e} = \int_V \rho_0 u_{e,r} b g \, dV. \quad (27)$$

This gives the global balance of energy in the split formulation

$$P_{Cor} + P_{buoy,e} = D_\nu + D_\kappa. \quad (28)$$

Note that this final balance is obtained by substituting the buoyancy power, P_{buoy} , by its saturation balance in the heat equation, $P_{buoy} = P_{buoy,e} - D_\kappa$, which accounts for the impact of thermal dissipation on the available power for the tidal flows.

2.3. Parameter space corresponding to resonant g-modes for a neutron star binary

Previous linear studies have shown that g-modes could be resonantly-excited in a neutron star binary. We build on the study by Suvorov et al. (2024b) for our NS models constructed with the APR4 EOS (Akmal et al. 1998) coupled to a Douchin and Haensel (DH) crust (Douchin & Haensel 2001). For our tests of both linear (Section 3) and non-linear calculations (Section 4), we study the resonance of g-modes in a $2.0M_\odot$ NS, where the frequency of the first g-mode is $N = 102.89$ Hz. We also consider an equal mass binary, so that the characteristic frequency is $\omega_d = 2288$ Hz for both stars. We vary the rotation rate Ω_s in this study with $\Omega_s = \frac{100}{\pi}$ Hz being a ‘‘standard’’ value. The resonant gravity, inertial, or mixed gravito-inertial modes are well-separated from ω_d and lie in the low-frequency regime. In addition, the tidal amplitude is as small as $\epsilon \sim 10^{-3}$ near the g-mode resonance when $2\Omega_o \sim N$. According to previous studies on inertial modes (Astoul & Barker 2022, 2023), this places us firmly in the linear regime but this could change for a lower viscosity, higher aspect ratio ($\alpha > 0.5$), or for the resonant gravito-inertial modes with the highest kinetic energy.

With respect to dissipation, we choose our standard viscosity and thermal diffusivity to be $\nu = \kappa = 10^{-6} R_o^2 \omega_d \approx 1.7 \times 10^{10} \text{ cm}^2 \text{ s}^{-1}$, similar to Pontin et al. (2023, 2024). This value is many orders of magnitude higher than the microphysical viscosity expected in NSs (Thompson & Duncan 1993) but is chosen to prevent numerical issues. These choices give an Ekman number of

$$Ek \equiv \frac{\nu}{R_o^2 \Omega_s} \approx 7.2 \times 10^{-5}. \quad (29)$$

The control parameter for the BV frequency in the simulations is the Rayleigh number, defined as

$$Ra \equiv -\frac{N^2 R_o^4}{\kappa \nu} \approx -2.02 \times 10^9. \quad (30)$$

As an astrophysical application, we study a more standard equal-mass neutron star binary of $1.6M_\odot$ in Section 5. The characteristic frequency is then $\omega_d = 1941$ Hz. We also use a ‘‘realistic’’ BV frequency and its value at the outer boundary to define the the Rayleigh number. The dimensionless numbers are $Ra = -5.1 \times 10^{10}$ and $Ek = 6.2 \times 10^{-5} - 1.99 \times 10^{-5}$ with a rotation rate of $\Omega_s = \frac{100}{\pi} - 100$ Hz, respectively.

2.4. Numerical methods

To solve the linear equations, we use the spectral MHD code DedaLus3 (Burns et al. 2020). DedaLus has been used to handle

different types of hydrodynamical and MHD problems, including convection, waves, and magnetic fields in an unstratified or stratified medium in many studies (Lecoanet et al. 2017; Couston et al. 2018; Ji et al. 2023). Using the full formulation, we benchmarked the code results against the study by Pontin et al. (2023) and are therefore confident of its results for when we will use the split formulation. The resolution used for the linear problem was $(n_r, n_\theta) = (200 - 400, 200 - 400)$ depending on the parameters.

In order to integrate the non-linear equations in time, Eqs. (17)–(19), we use the benchmarked pseudo-spectral code MagIC (Wicht 2002; Gastine & Wicht 2012; Schaeffer 2013). MagIC solves the 3D MHD equations in a spherical shell using a poloidal-toroidal decomposition for the velocity and the magnetic field (made possible by the solenoidal assumption on \mathbf{u}),

$$\rho_0 \mathbf{u} = \nabla \times \nabla \times (W \mathbf{e}_r) + \nabla \times (Z \mathbf{e}_r), \quad (31)$$

$$\mathbf{B} = \nabla \times \nabla \times (b \mathbf{e}_r) + \nabla \times (a_j \mathbf{e}_r), \quad (32)$$

where W and Z are the poloidal and toroidal kinetic scalar potentials, respectively, while b and a_j are the magnetic potentials. The scalar potentials and the pressure P are decomposed on spherical harmonics for the colatitude (θ) and the azimuthal (ϕ) angles, together with Chebyshev polynomials in the radial direction. For more detailed descriptions of the associated spectral transforms and the numerical method, we refer to Gilman & Glatzmaier (1981), Tilgner & Busse (1997), and Christensen & Wicht (2015).

The simulations presented in this paper were performed using a standard grid resolution of $(n_r, n_\theta, n_\phi) = (257, 256, 512)$. Some of the simulations have a cutoff m_{max} in the spherical harmonics to speed up the simulations; for simulations in Section 4, $m_{max} = 85$ is enough to ensure convergence as the dominant mode corresponds to $m = 2$.

3. Linear tests of the formulation

In this section, we test the new split formulation. As a first step, we show that we are able to reproduce the properties of g-modes obtained with the ‘‘full’’ formulation (Sec. 3.1). This sets us up to study gravito-inertial modes to check whether the two effective tidal forcings give the correct geometry and amplitude of the gravito-inertial modes (Sec. 3.2). In order to compare more easily with Pontin et al. (2023), we adopt in this section the same units as that study: $R_o = 1$, $\omega_d = 1$ and $\rho_0 = 1$.

3.1. Pure g-modes

As a benchmark of the DedaLus code and the full and split formulations, we first consider non-rotating stars ($\Omega_s = 0$) and also fix $N^2 = 1$ and $\Psi_0 = 1$. For the split formulation, we further use a dimensionless tidal amplitude $C_t = \Psi_0 / \omega_d^2 = \sqrt{6\pi/5} \epsilon = 1$ in this section. We then solve the linear system for both the full formulation and split formulation. In order to verify that mode resonances behave the same, we first plot the kinetic energy as a function of the tidal forcing frequency $\hat{\omega} = 2\Omega_o$. Fig. 1 shows that the dissipation peaks reside at the same frequencies until the tidal forcing frequency becomes close to the f-mode frequency, $\omega_d = 1$. This shift was found in Pontin et al. (2023), where the pure g-mode frequencies computed were slightly off the resonant frequencies, with disagreement growing as one approaches ω_d . The split formulation recovers, with high accuracy ($< 0.4\%$), the theoretical frequencies of $\ell = m = 2$ g-modes (${}_n g_2^2$ for radial node-number n); in a cavity for a constant BV frequency N ,

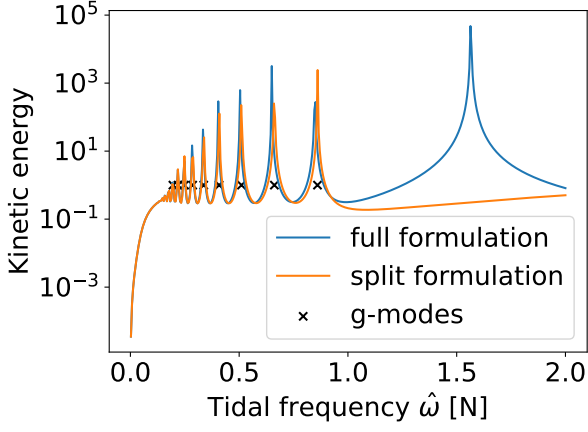
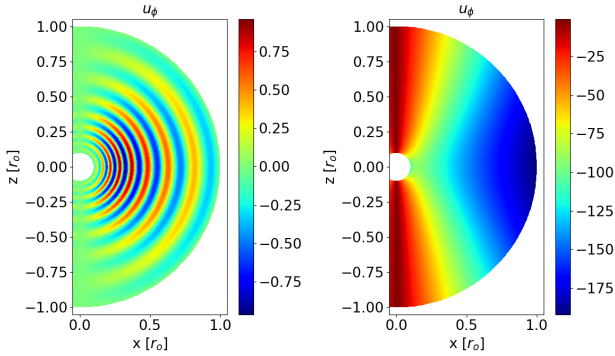


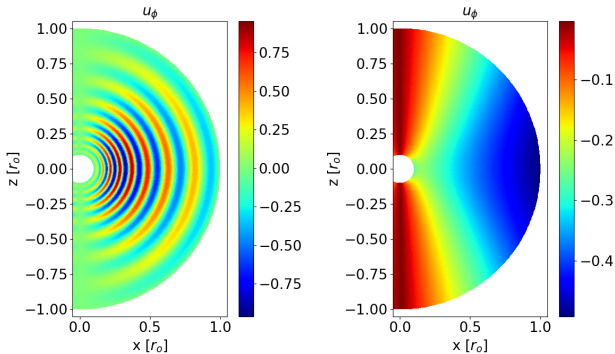
Fig. 1: Kinetic energy as a function of the tidal frequency $\hat{\omega}$ depending on the formulation used (see plot legends). Crosses correspond to the g-mode frequencies in a cavity (Equation (B9) of Pontin et al. 2023). Code units are used such that $R_o = 1$, $\omega_d = 1$, and $\rho_0 = 1$.

these are given by Pontin et al. (2023)

$$\omega_{n8_2^\ell}^2 = \frac{4l(l+1)N^2(\ln(\alpha R_o))^2}{(2l+1)^2(\ln(\alpha R_o))^2 + 4\pi^2 n^2}. \quad (33)$$



(a) Toroidal velocity u_ϕ in the full formulation for $\hat{\omega} = 0.1$ (left) and $\hat{\omega} = 1.56$ (right) at $\phi = 0$.



(b) Toroidal velocity u_ϕ in the split formulation for $\hat{\omega} = 0.1$ (left) and $\hat{\omega} = 1.56$ (right) at $\phi = 0$.

Fig. 2: Comparison of the azimuthal eigenfunctions for resonant modes in the full formulation (top) and the split formulation (bottom) for two representative $\hat{\omega}$ (see subcaptions).

In addition to the characteristic frequencies of g-modes, the split formulation in the regime where $\hat{\omega}$ is far from ω_d is similarly able to reproduce the eigenfunction of the resonant mode obtained by the full formulation to very high accuracy, within $< 0.01\%$ (left panels of Figure 2). However, when the tidal forcing frequency $\hat{\omega}$ is of the same order of magnitude ω_d , the split formulation cannot reproduce the resonance as it is expected. Indeed, the split formulation cannot reproduce f-modes as the surface needs to be free.

3.2. Gravito-inertial modes

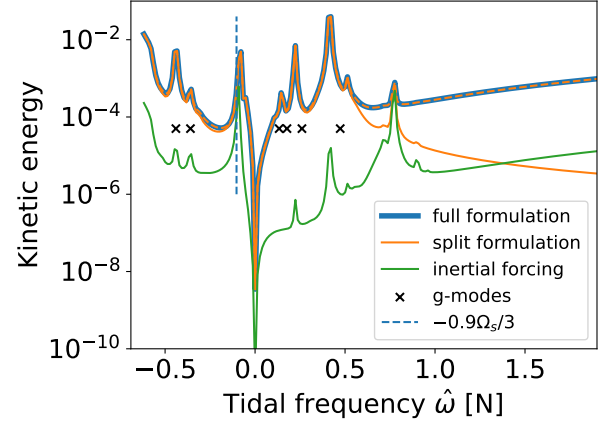
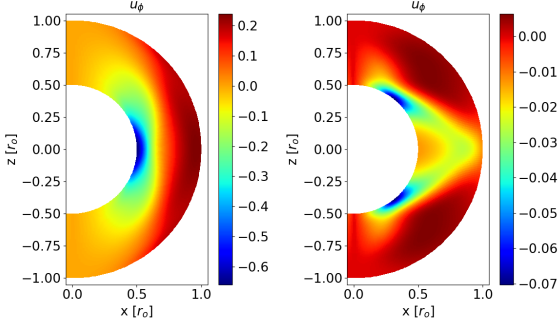


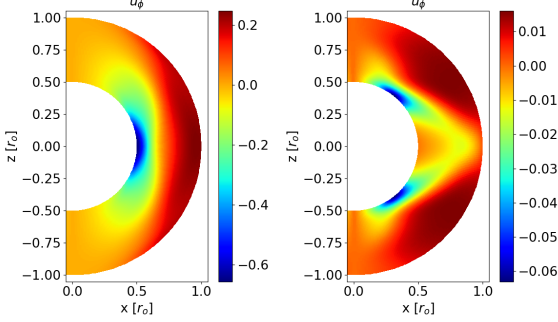
Fig. 3: Kinetic energies of tidally-excited fluid motions as functions of the tidal forcing frequency $\hat{\omega}$ when the full tidal potential is taken into account (blue) and when the tidal forcing is effectively described using the equilibrium tidal flow (orange). The orange dashed line also corresponds to the split formulation but with different boundary conditions (see text), while the solid, green line corresponds to the modes obtained only with the effective tidal forcing f_t due to Coriolis force. Pure g-modes frequencies (black, Eq. 33) and negative g-modes (red) are designated by a cross. A Rossby mode resonance is highlighted at $\hat{\omega} = -0.9\Omega_s/3$.

We apply the split formulation to tidal resonance problem for low-frequency modes in rotating neutron stars, where inertial modes, and gravito-inertial modes also come into play. We are therefore in the regime where $\hat{\omega} \ll \omega_d$ and $\Omega_s N \ll \omega_d$. For our second test, we want to probe the impact of the rotation on the gravity modes (i.e. to compare g-modes with gravito-inertial modes) in the right parameter regime. We set $\Omega_s = 0.0139 \omega_d$ and $N = 0.0450 \omega_d$, respectively.

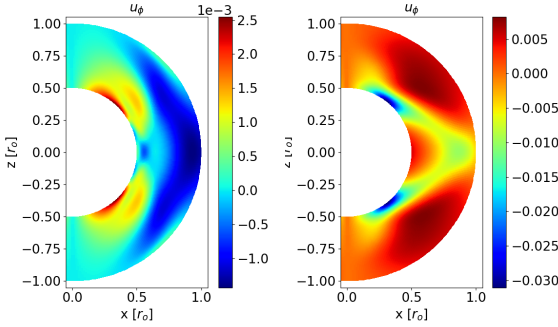
With these parameters, we compute the kinetic energy of the resonant modes depending on the tidal frequency for the two formulations. Since we are far away from the respective f-mode frequencies, we find that the peak kinetic energy frequencies are identical for both formulations (Figure 3). We also find that the range of gravito-inertial mode is roughly $[-2\Omega_s, N]$, which is consistent with the limit $\hat{\omega}_{max} = N\sqrt{1 + 4\Omega_s^2/N^2} \approx 1.18N$ found in previous studies (Rieutord 2009; Pontin et al. 2024). By looking at their radial wavelengths, we identify the gravito-inertial modes corresponding to the pure g-modes $4g$ to $1g$ with slightly smaller frequencies compared to Eq. (33) in the positive frequencies and from $3g$ to $2g$ modes in the negative frequencies. We find that these negative modes corresponding to $n = 2$ and $n = 3$ seems to be roughly at frequencies corresponding to



(a) Toroidal velocity u_ϕ at $\phi = 0$ in the full formulation for $\hat{\omega} = 0.421N$ (left) and $\hat{\omega} = 0.777N$ (right).



(b) Toroidal velocity u_ϕ at $\phi = 0$ in the split formulation for $\hat{\omega} = 0.421N$ (left) and $\hat{\omega} = 0.777N$ (right).



(c) Toroidal velocity u_ϕ at $\phi = 0$ with only the effective Coriolis forcing f_i for $\hat{\omega} = 0.421N$ (left) and $\hat{\omega} = 0.777N$ (right).

Fig. 4: Comparison of two gravito-inertial modes along $\phi = 0$ for the different formulations. The first mode, with $\hat{\omega} = 0.421N$, corresponds to the $1g_2^2$ mode impacted by the rotation, while the second one is closer to an inertial or gravito-inertial mode, $\hat{\omega} = 0.777N$. Velocities are given in units such that $R_o\omega_d = 1.56 \times 10^{10} \text{ cm s}^{-1}$.

$\hat{\omega}_{n g_2^2} \approx -\omega_{n g_2^2} - \frac{3}{5}\Omega_s$ (i.e. rotation breaks symmetry; in the non-rotating case, negative g-modes are perfectly symmetrical to the positive as in Pontin et al. 2023). The peak at the lower limit of frequencies $\hat{\omega} = -2\Omega_s$ is related to the negative $1g$ mode but the resonance peak seems not to be reached (not shown here). We also identify a resonant mode close to the frequency of a resonant Rossby mode at $\hat{\omega} = -0.9\frac{\Omega_s}{3}$. The usual frequency for this resonance is $\hat{\omega} = -\Omega_s/3$ but it is expected to decrease with α (Ogilvie 2009; Pontin et al. 2024). The identification of the resonant modes with $\hat{\omega} > \omega_{1g_2^2} \approx 0.47$ is not straightforward since they cannot be predicted from Eq. (33) and thus are not slightly shifted g-modes. For these other modes, the presence of stratification, which has the effect of shifting resonant peaks

(compared to neutrally-stratified studies), does not allow clear comparison with any of the regular or singular inertial modes of Ogilvie (2013) or Astoul & Barker (2023). The next resonant peak corresponding to $\hat{\omega} \approx 0.51$ seems to be a gravito-inertial mode as it has some mixed g-mode and inertial mode features and the $n = 1$ radial wavelength. This mode is still in the sub-inertial range $\hat{\omega} < 2\Omega_s$ where we expect to find equatorially trapped hyperbolic gravito-inertial modes (as described in Dintrans et al. 1999; Dintrans & Rieutord 2000; Mathis 2009). The higher frequency peaks with $\hat{\omega} > 2\Omega_s$ (in the super-inertial regime) presumably belong to the elliptic gravito-inertial mode family, as described in the aforementioned studies.

We also compare the kinetic energy to the split formulation but without the forcing term f_N in the heat equation, so just with f_t which we call inertial forcing (green line on Figure 3). Some of the peaks linked to the stable stratification and g-modes cannot be seen anymore, are strongly mitigated (especially for low frequency), or change geometry completely as shown on the $1g$ mode (left panel of Figure 4). Without it, it corresponds to having gravito-inertial modes with the gravity component only secondarily excited by the effective Coriolis forcing. For example, the mode at $\hat{\omega} = 0.777N$ is well recovered with only the effective Coriolis forcing although the amplitude is divided by two (right panel of Figure 4 but at the frequency of the $1g$ mode the mode is completely different (left panel of Figure 4).

For all the peaks below $\hat{\omega} < 0.5N$, the kinetic energy for both formulations agrees within $< 1\%$ but there are some differences with the full formulation as the amplitude of the velocity becomes lower in the split formulation for the tidal frequencies $\hat{\omega}$ larger than the BV frequency. This means that some tidal response seems to not be captured by the split formalism when further away from the g-mode or gravito-inertial mode frequencies. In order to investigate this effect, we look at the resonant mode for two different tidal forcing frequencies. For $\hat{\omega} < N$, the gravito-inertial mode velocity is reproduced within 0.5% by the split formulation (two upper left panels of Figure 4). We can also see the impact of the rotation, which makes the mode more cylindrical than the spherical symmetry of pure g-modes. For $\hat{\omega} \approx N$, the toroidal velocity is not exactly reproduced by the split formalism, and the kinetic energy seems to decrease with increasing tidal frequency since we leave the allowed frequency range for gravito-inertial waves to be excited and equilibrium tide is not negligible anymore. This behavior can be explained by differences in the boundary conditions. Indeed, when outside of the resonant peaks, the amplitude of the equilibrium tide \mathbf{u}_e cannot be neglected compared to those of the dynamical tide \mathbf{u} . This leads to a difference in boundary conditions as the full formulation solve the equations for both tides $\mathbf{u} + \mathbf{u}_e$, while the split formulation solve the equation for the dynamical tide \mathbf{u} . In order to compare the two formalisms, we artificially take into account the impact of the equilibrium tide by changing our boundary conditions for the viscous rate tensor to $\tau_{v,r\theta}(\mathbf{u}) = -\tau_{v,r\theta}(\mathbf{u}_e)$ and $\tau_{v,r\phi}(\mathbf{u}) = -\tau_{v,r\phi}(\mathbf{u}_e)$. Applying these changes, we recover the results from the full formulation within $< 0.05\%$ (Figure 5).

Since the split formulation has two effective forcing terms, f_t and f_N , we can compute the power associated with both to assess their importance. Figure 6 shows the different components of the power of the forcings and the thermal and viscous dissipation due to the tidal flows. We first verify that the balance of Equation (28) is verified and the error that depends on resolution is around of $10^{-7}\%$. For almost all the modes, the power of the forcing f_N due to the advection of the buoyancy variable gradient dominates, which is expected since we are in the regime $N > \Omega_s$. It even dominates at a resonant Rossby frequency $\hat{\omega} = -\Omega_s/3$

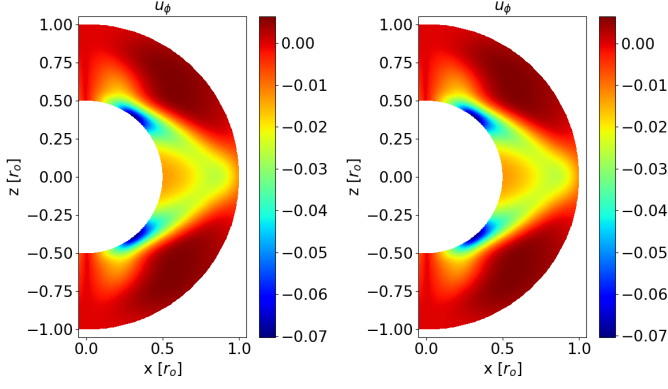


Fig. 5: Toroidal velocity u_ϕ with $\hat{\omega} = 0.777N$ in the full formulation (left), and in the split formulation (right) with modified non stress-free boundary conditions (see text).

where the contribution of the effective Coriolis forcing is the strongest for negative frequencies and is around $P_{Cor} \approx 0.4P_{buoy}$. The only exception is of the gravito-inertial modes found for $\hat{\omega} = 0.777N$, described before. We also find that the power due to the Coriolis effective forcing f_t alternates between negative and positive values. This may be linked to the splitting due to rotation of the gravity modes $m = 2$ and $m = -2$.

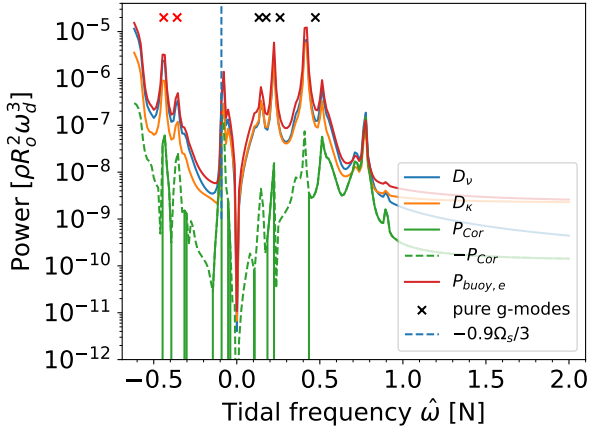


Fig. 6: Power/dissipation balance of the tidally-excited fluid motions as function of the tidal forcing frequency $\hat{\omega}$ with the split formulation of the tidal forcing with $N/\Omega_s = 3.24$. Similar to Figure 3, the modes are designated by crosses.

The case of pure inertial modes with the effective body force f_t has been well studied and therefore needs no testing. Overall, these tests show that the split formulation with the two forcing terms is able to obtain well the resonant gravito-inertial modes without having a free surface implemented.

4. Non-linear simulations of gravito-inertial modes

As the orbital separation a shrinks with time due to the emission of GWs, the tidal forcing frequency and amplitude increase, and non-linear effects can start to be important for the dynamics of the resonance. In this section, we wish to test and study the importance of non-linear effects for binary NSs. In particular, we now need to look at the non-linear saturation of the gravito-

inertial modes (i.e. when the non-linear simulation reach an average steady state).

We implement the split formulation in the code MagIC with the stress-free conditions applied to the dynamical tide \mathbf{u} , since it does not change results for resonant modes. In a similar fashion to Astoul & Barker (2023), we also choose to neglect some non-linear interactions between the equilibrium and dynamical tides. Indeed, our model uses a non-deformed spherical shell which, in the presence of mixed (equilibrium-dynamical) nonlinear terms, would lead to a non-vanishing equilibrium tide at the surface $\mathbf{u}_e \cdot \mathbf{n} \neq 0$. In this case, the advection of the dynamical flow by the equilibrium flow artificially generates angular momentum and spin-up the star. We, therefore, neglect this advection term to avoid this setup artifact and because it is justified in the astrophysical regime (see discussion of Astoul & Barker 2022). For the saturation of the flow, we only consider the non-linear effects of the dynamical tide on itself $(\mathbf{u} \cdot \nabla)\mathbf{u}$.

We use this implementation to run several simulations for a NS binary of 2 solar masses adopting an initial rotation of $\Omega_s = 100/\pi$ Hz to continue the comparison as in the previous section. One notable difference is that, in this section, the gradient of buoyancy variable $\frac{db}{dr} \propto \frac{N}{g}$ is constant instead of the BV frequency for the sake of simplicity. The BV frequency now depends on the radius and we have $N(r) = Nr$ and $g = g_o r$.

For the amplitude of the tidal force, we choose the tidal parameter to reflect the situation of having $\hat{\omega} \approx N$ so as to study the resonance of gravito-inertial modes, which gives a tidal amplitude of $C_t \approx 10^{-3}$ for $N = 102.87$ Hz, $\Omega_s = 100/\pi$ Hz, and $\omega_d = N/0.0450$. In order to investigate differences in non-linear effects between the different modes, we keep the tidal amplitude constant for all simulations in this section. Note that we would have $C_t = \sqrt{6\pi/5}\epsilon \propto (\Omega_o/\omega_d)^2$ (neglecting the real part of the Love number) in the realistic case (see Section 5).

4.1. Linear and non-linear comparison

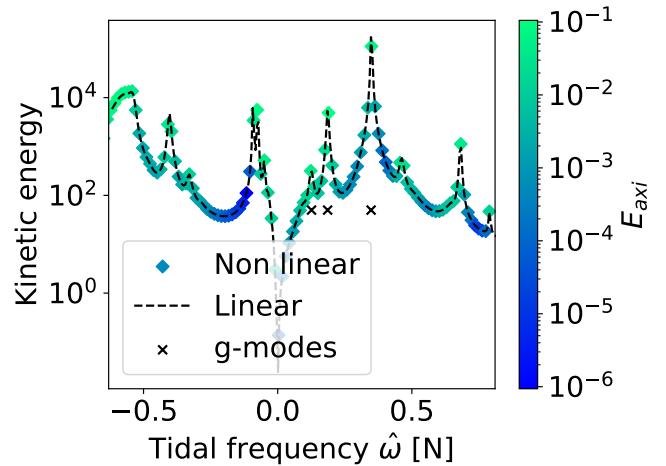


Fig. 7: Kinetic energy along the tidal frequency $\hat{\omega}$ for the linear code (dashed lines) or the non-linear simulations (scatter points). The colour scale of the non-linear simulations corresponds to the ratio of the axisymmetric kinetic to the total kinetic energy.

To be confident in our non-linear simulations, we first compare the MagIC simulation results to the linear results. We run the linear code for $\hat{\omega} \in [-2\Omega_s, 2N]$ with a frequency resolution

$N_{freq} = 500$, while $N_{freq} = 100$ for the non-linear simulations. Figure 7 shows the total kinetic energy of the different modes for both the linear code and the non-linear code MagIC. Overall, we find a good agreement between the two codes for many resonant modes, and the comparison of one of these cases can be seen for the $3g$ mode (first mark furthest to the left on Figure 7) in Figure 8. The mode is deformed by rotation and becomes more cylindrical compared to a pure g-mode (see left panels of Figure 2 for a pure g-mode at a different frequency). We still notice small differences for some resonance modes, but such effects may stem from the two different frequency resolutions or due to small non-linear effects.

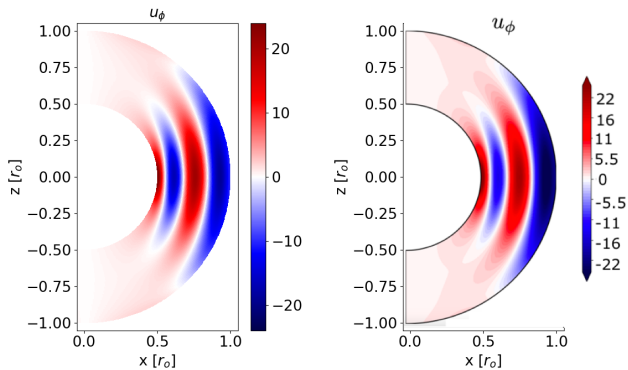


Fig. 8: $3g$ -mode resonance at $\phi = 0$ in the case of small rotation ($N/\Omega_s = 3.24$). Results of the linear code are shown on the left, while that of the non-linear code are on the right; notice the difference in the color bar for each panel.

To quantify the importance of non-linear effects, Figure 7 shows the ratio of the axisymmetric-to-total kinetic energy in these simulations. It clearly shows that with the strongest resonance modes, a $m = 0$ zonal flow component emerges in addition to the forced $m = 2$ component. This means that non-linear effects are stronger for these modes. It is not the only criterion though, as the $2g_2^-$ mode has the highest percentage of axisymmetric energy, while the $1g_2^-$ mode has the highest mode energy.

4.2. Non-linear saturation

The previous section showed that for $C_t = 10^{-3}$ the non-linear saturation of the kinetic energy matches the linear one. In this section, we examine this assumption to see if it still holds for the strongest resonances. Since non-linear effects could become important, we also compare the linear and non-linear simulations for cases with the highest percentage of axisymmetric energy and the highest absolute axisymmetric energy. They correspond to the $2g^-$ and $1g$ modes, as discussed above. We first check that in the case of $C_t = 10^{-9}$, the kinetic energy of both non-linear simulations agree with the associated linear simulations within a relative error $< 10^{-6}$. Figure 9 compares the time evolution of the non-linear simulations and the saturated energies predicted by the linear calculations for both modes. We find that the non-axisymmetric energy of the $2g$ -mode agrees well with the linear kinetic energy. We note that its total saturation is slightly increased by the axisymmetric energy, which is 10% of the total energy. In the case of the $1g$ -mode, the non-linear saturation is lower by a factor 3. This means that the saturation mechanism differs from the linear theory for this mode. It is possible that we only see it for this mode due to it having the strongest amplitude.

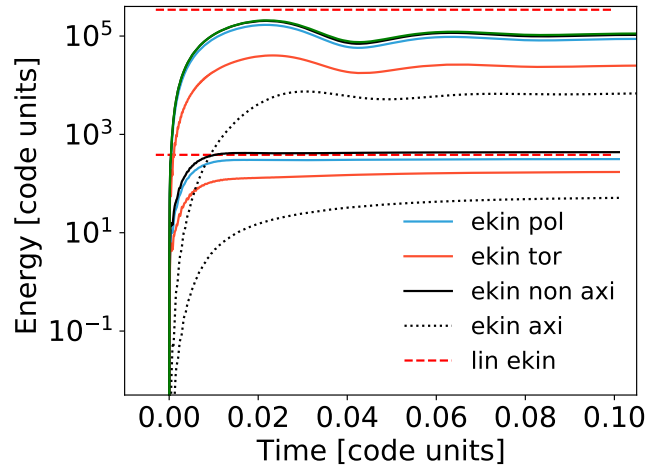


Fig. 9: Time evolution of the kinetic energy for the non-linear simulations of $1g$ and $2g$ modes compared to the linear saturations (dashed red lines). The above lines correspond to the $1g$ mode and below lines $2g^-$ mode, which have been rescaled by a factor 0.1 for improved visibility.

Figure 10 compares the non-axisymmetric and axisymmetric toroidal velocity of the two modes to see the impact of the non-linear saturation. We find that axisymmetric rotation, decreasing with cylindrical radius, is generated for both modes. We expect that the differential rotation emerges due to non-linear processes such as tidal wave-wave interactions ($m = 2$ and $m = -2$ non-linear coupling to form an $m = 0$ mode, as explained in Barik et al. 2018; Astoul & Barker 2022, for inertial waves) and/or wave breaking as in Barker & Ogilvie (2010) in a 2D cylindrical geometry, Barker (2011) in a 3D box, and Guo et al. (2023) in a 2D circular cavity (see also e.g. Semin et al. 2016, for experimental generation of a mean flow by internal gravity waves). In the latter, the geometrical focusing of gravity waves launched from the surface towards the center generates differential rotation from inside out by wave breaking (or weak linear damping) of (subcritical) waves and their progressive deposition of angular momentum. From the simulations presented here, the presence of both Coriolis and buoyancy forces promotes a mix between cylindrical and spherical geometry of the mean flow (which is reminiscent of latitudinal differential rotation produced in Fig. 6 of Barker 2011). In proportion to the amplitude, the differential rotation is stronger for the $2g$ -mode.

The emergence of differential rotation supports the ability of the resonant mixed gravito-inertial modes to be able to amplify some ambient magnetic field through winding in a way that is qualitatively similar to that studied by Astoul & Barker (2025). In future work, these results should be checked for different BV frequencies that are more realistic for astrophysical sources to assess the impact of the differential rotation amplitude.

5. An astrophysical application: gravito-inertial modes in a neutron star binary

Depending on the stellar spin, the eigenfrequencies of gravito-inertial modes imply that they may become resonant some seconds prior to merger in a binary neutron-star inspiral. Because of their polar character, the leading-order overlap integrals and hence amplitudes may also be sizeable. These aspects together

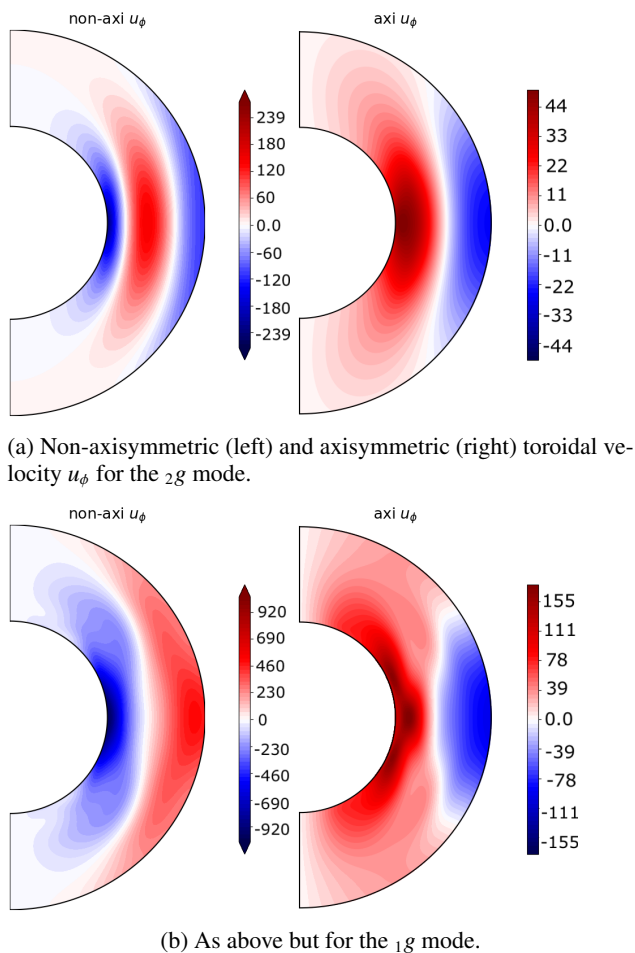


Fig. 10: Strongest two g -mode resonances and their non-linear saturation in the case of small rotation ($N/\Omega_s = 3.24$).

indicate that these modes may be important in the description for mergers for a few reasons:

- ★ A leading theory for explaining the ignition of GRB precursor flares, seen in $\lesssim 5\%$ of mergers (Coppin et al. 2020; Wang et al. 2020), is that of crustal failure: resonant modes exert strain on the ion lattice defining the crust, which may exceed its elastic maximum if the mode amplitudes are large enough. Such an overstraining relieves the star of some magnetoelastic energy, which can fuel a gamma-ray flash (Tsang et al. 2012). Previous estimates using a linear, general-relativistic (GR) framework (Passamonti et al. 2021; Kuan et al. 2021b; Suvorov et al. 2022) found that some g -modes may exceed modern estimates for polycrystal strain maxima (Baiko & Chugunov 2018; Baiko 2024); a direct comparison is made with our nonlinear models in Sec. 5.1.
- ★ Energy may be siphoned from the orbit into the kinetic energy of the modes, leading to GW dephasing. Linear theory predicts that while the dephasing due to gravity(-inertial) modes is unlikely to be visible to current interferometers, it may be relevant for next-generation ones (Ho & Andersson 2023, see also Suvorov et al. 2024a). In general, however, we expect that treating mode excitations via non-linear perturbation theory would favour measurability since amplitudes in post-resonance regimes do not remain constant as in linear theory (Yu et al. 2024; Kwon et al. 2024, 2025). In addition, the onset of GW dephasing depends on the resonance

timing, which will differ between linear and nonlinear models, as explored in Sec. 5.1. Deducing their non-linear saturation amplitudes is a necessary step towards providing realistic assessments of dephasing; such a comparison is made in Sec. 5.2.

- ★ Observations of nonthermal GRB precursors and other aspects (see, e.g. Xiao et al. 2024) hint that some magnetar-like objects participate in a rare subclass of merger. This is difficult to reconcile with the fact that Ohmic decay times are thought to be much shorter than a characteristic inspiral time (e.g. Pons & Viganò 2019). One solution is that actually strong fields are not preserved but rather generated prior to coalescence by a mode-driven dynamo, as suggested by Suvorov et al. (2024b). The validity of this scenario depends on microphysical specifics as well as the mode properties; some MHD aspects of this in the context of the simulations presented here are discussed in Sec. 5.2.2.

In this section, we wish to come back closer to the astrophysical objects of a standard NS binary. For that, we change our model and consider a more standard NS of $1.6M_\odot$, anticipating that for objects with non-negligible spin some prior epoch of accretion may have increased the birth value. We now take a radial profile for the BV frequency inspired by a realistic model of the NS from Suvorov et al. (2024b). We neglect (physical) discontinuities arising in the BV frequency in our “crustal cavity” due to different layers of nuclear composition, as results are very likely to change with density variations between the core and the crust. The study of core-crust interfacial modes (i.e. i -modes; Tsang et al. 2012) due to these discontinuities is left to future studies. In Figure 11, we show the smoothed BV frequency: it is visually identical to that predicted by the GR calculations except in the crust. The other main difference in our non-linear simulations from the linear calculations in Suvorov et al. (2024b) would be that the density is still kept constant, as we first aim to understand non-linear effects in a simpler setup.

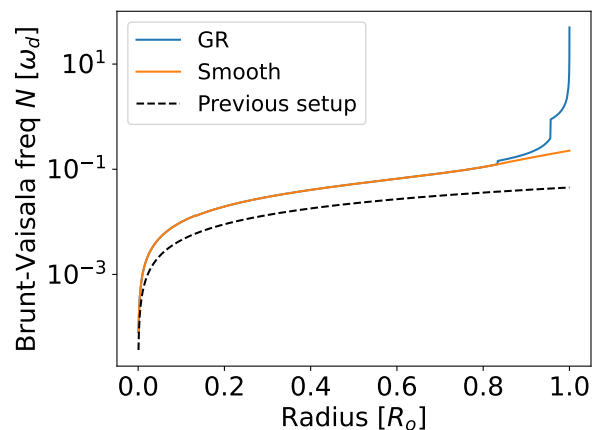


Fig. 11: BV frequency for a $1.6 M_\odot$ NS with the APR4 EOS, giving a radius of $R_o = 11$ km from Suvorov et al. (2024b). The orange line is the profile that is used in the Newtonian simulations presented here (see main text for details). For reference, we overlay the BV frequency of the setup in Sec. 4 (dashed line).

5.1. Comparison to GR linear calculations

First, before treating rotation self-consistently, we can directly compare GR linear calculations to our linear ones to estimate the

impact of our numerical hypotheses. To compute these modes, we use a radius ratio of $\alpha = 0.1$ and the smooth BV profile from Fig. 11. As it turns out, the agreement is encouraging: the resonant frequencies are only slightly shifted to lower or higher values by 3.5% and 2.3% for the $2g$ and $1g$ modes, respectively.

The radial eigenfunctions between the two also agree well until a radius of $\approx 0.8R_o$, where the impact of the density gradient and, subsequently, the discontinuities become more important (see Figure 12 for the case of u_ϕ , which corresponds to u^ϕ in GR calculations). In terms of amplitudes, the Newtonian $1g$ and $2g$ modes are rescaled by a factor of ~ 0.02 and ~ 0.0175 for the radial profiles to match, respectively. This rescaling is due to the way the linear modes are computed: in the GR case, the saturation is determined by the resonance time window, while, in the Newtonian case, the saturation is determined by the diffusivities. The rough agreement between the rescaling factors shows that the results from the Newtonian case in the core are consistent with the GR linear calculations. We can therefore use the smooth BV frequency to study the resonant modes and their non-linear saturation. However, the results will be mostly relevant to core-like regions of the NS, and a proper treatment of the density and BV discontinuities is required to study quantitatively the modes in the crust.

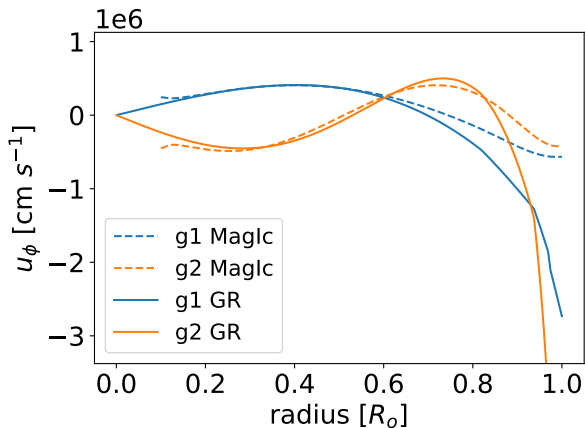


Fig. 12: Toroidal velocity for $1g_{22}$ and $2g_{22}$ modes. Solid lines represent the cases as those in Fig. 1 of Suvorov et al. (2024b).

5.2. Non-linear saturation of the strongest resonance

In this section, we test the impact of rotation on the $1g$ and $2g$ modes that generate the strongest non-linear differential rotation in Section 4.2. We first start with the $2g$ mode as it has the lowest tidal amplitude so non-linear effects are expected to be smaller. We therefore consider three different rotation rates $\Omega_s \in [0, 100/\pi, 100]$ Hz (i.e., astrophysically corresponding to irrotational, moderate, or “recycled” objects). To keep the viscosity the same as previous simulations, the same Rayleigh number Ra is maintained but the Ekman number now, respectively, varies from $Ek = 6.2 \times 10^{-5}$ to $Ek = 1.99 \times 10^{-5}$ in the slow and fast rotating cases (note that the Ekman number is not defined for $\Omega_s = 0.0$). With the new BV profile, which is normalized at the outer boundary, the Rayleigh number is now $Ra = -5.1 \times 10^{10}$. For the same tidal forcing frequency, the orbital frequency Ω_o is effectively higher since the spin of the NS is increased, and thus we have a larger tidal amplitude parameter ϵ . Our strategy is to first use the linear code to compute the resonant fre-

quencies which is fed into the non-linear code to compute the saturation amplitudes. As one of our motivations is to investigate the strength of the magnetic field that could be theoretically generated by differential rotation, energies are shown in ergs and compared to the strength of a magnetic field that would have the same energy as the flow kinetic energy. This comparison is done by using the energy of uniform 10^{14} G magnetic field, $E_{B14} = \frac{1}{8\pi} [(10^{14}\text{G})^2 V] = 2.27 \times 10^{45}$ erg, where $V = \frac{4\pi}{3}(1 - \alpha^3)R_o^3$ is the volume of the domain.

5.2.1. $2g$ mode

We first start with the description of the $2g$ mode for different rotation rates, $\Omega_s \in [0, 100/\pi, 100]$ Hz. For these spins, the tidal forcing frequencies of the $2g$ mode are respectively $\hat{\omega}/N \in [0.146, 0.132, 0.127]$ while the tidal dimensionless amplitudes are $C_t = 9.3 \times 10^{-4}$ and $C_t = 4.1 \times 10^{-3}$ for the two rotating cases. In order to compare the efficiency of the non-linearities in the non-rotating case, we manually adjust the tidal amplitude in the non-rotating case to the fast rotating case, namely $C_t = 4.1 \times 10^{-3}$ instead of the realistic one $C_t = 5.29 \times 10^{-4}$. This allows us to effectively mimic non-linear effects at lower viscosities since the amplitude of the resonant modes increases with decreasing viscosity (in the linear regime, e.g. Ogilvie 2009; Pontin et al. 2023). Figure 13 shows the time evolution of the different kinetic energies, which for all simulations would be enough to generate a magnetic field stronger than 10^{14} G if we assume that this kinetic energy would be subdivided through dynamical means into equal parts kinetic and magnetic energy (equipartition). We see that non-linearities become relevant for both modes after less than 1 s of evolution. The non-linearities for the $2g$ mode and their impact are mostly seen in the toroidal kinetic energy which is expected physically as zonal flows mainly develop in the azimuthal direction. For $\Omega_s = 100/\pi$ Hz, the poloidal kinetic energy dominates and non-linear effects are weaker than the other case due to the lower tidal amplitude. We find that the axisymmetric energy represents $\sim 20\%$ of the total kinetic energy. This is higher than but still consistent with the results of the previous section. For a faster star with $\Omega_s = 100$ Hz, the toroidal component becomes dominant and the axisymmetric kinetic energy is comparable to the non-axisymmetric energy, representing $\sim 50\%$ of the total energy.

To understand whether this increase is due to rotation or the tidal amplitude, we compare it to the non-rotating case with the same tidal amplitude. We find a striking difference for $\Omega_s = 0$: the non-linear effects become important much faster, and the axisymmetric toroidal velocity becomes dominant after 1 s. The toroidal kinetic energy saturates at a higher level compared to the other two rotating cases. This different evolution may be due to the fact that the amplitude of linear g-modes also saturate at greater values with lower rotation because of overlap integral properties (see Figure 6 of Pontin et al. 2024). For a given tidal amplitude, the non-linear effects are therefore more important with lower rotation, which is what we observe in our simulations.

To compare the non-linear effects for the three cases in more detail, we look at the kinetic energy spectra along degrees ℓ and orders m . The $m = 2$ mode would dominate for purely linear solutions, and the $\ell = 2$ mode should dominate for pure g-modes as the different ℓ modes are only coupled by the Coriolis force. Note that $\ell = 2$ is also dominant for linear inertial waves due to the tidal potential have a $\ell = 2$ geometry. In addition, we expect to have even ℓ modes dominating for the poloidal field and odd

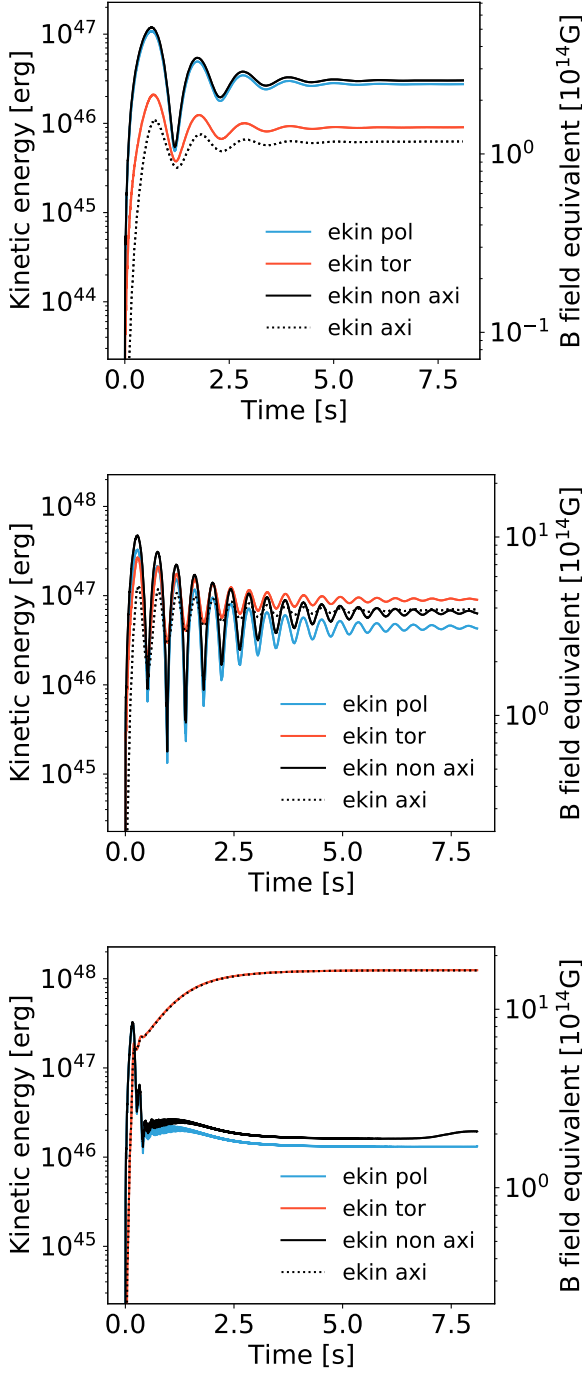
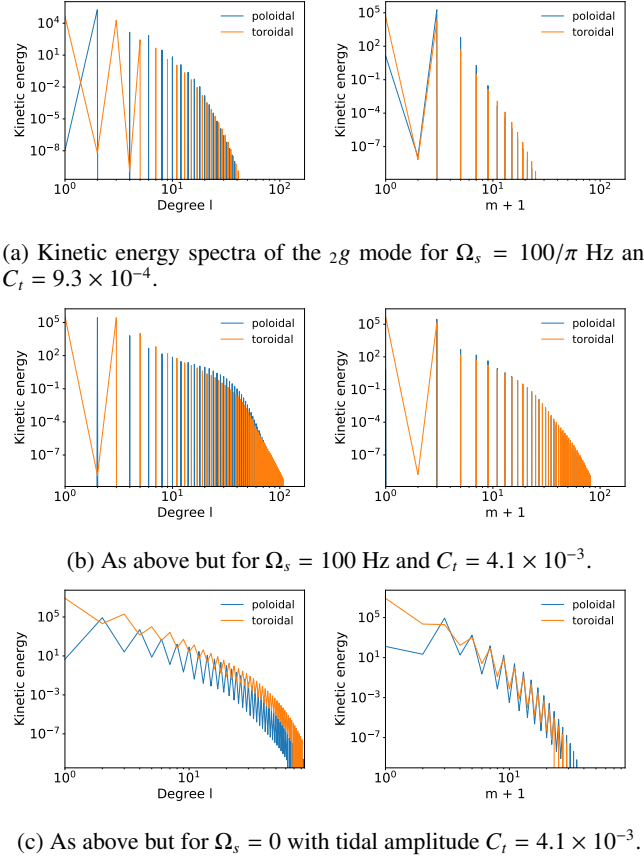


Fig. 13: Time evolution of the kinetic energy for the $2g$ mode for $\Omega_s = 100/\pi$ Hz, (top), $\Omega_s = 100$ Hz (middle), and $\Omega_s = 0$ with an increased tidal amplitude (bottom).

ℓ modes for the toroidal field due to the equatorial plane symmetry of the equilibrium tide used for the effective forcing. We see these behaviors in the spectrum depending on the ℓ modes of the two rotating cases and, to a lesser extent, in the non-rotating case too (left panels of Figure 14). As non-linear effects become more important (i.e., at higher tidal amplitudes), the spectrum gets extended to higher degrees ℓ .

For the spectrum along order m , we see that the $m = 2$ and the $m = 0$ modes dominate, respectively, for the poloidal component and for the toroidal component (right panels of Figure 14). We



(a) Kinetic energy spectra of the $2g$ mode for $\Omega_s = 100/\pi$ Hz and $C_t = 9.3 \times 10^{-4}$.

(b) As above but for $\Omega_s = 100$ Hz and $C_t = 4.1 \times 10^{-3}$.

(c) As above but for $\Omega_s = 0$ with tidal amplitude $C_t = 4.1 \times 10^{-3}$.

Fig. 14: Kinetic energy spectra of the $2g$ -mode resonance for $\Omega_s = 100/\pi$ Hz, (top), $\Omega_s = 100$ Hz (middle), and $\Omega_s = 0$ with an increased tidal amplitude (bottom). Left panels are kinetic energy integrated over r and m , while varying ℓ ; and right panels are integrated over r and ℓ , while varying m .

also see that odd orders m are non-relevant for the rotating cases and only start to become relevant for the non-rotating case with the strongest non-linear effects while being below even modes. We see that the amplitude of the toroidal mode $m = 0$ becomes more and more dominant as tidal amplitude gets higher, which is consistent with the ratio of axisymmetric energy in the time evolution. The $m = 0$ mode of the poloidal component stays much lower than the $m = 2$ mode.

To confirm the importance of the $m = 0$ mode of the velocities, we show snapshots of u_r and u_ϕ in the equatorial plane for the three different cases in Fig. 15. In the rotating cases, we see that the modes are quite similar: for u_r , the differences between the maximum amplitude of the dominant $m = 2$ mode are within 30%, and there is only a small difference in geometry close to the equatorial plane (not shown here). There are more differences for u_ϕ as its amplitude increases with rotation and tidal amplitude. The increase of the axisymmetric component with tidal amplitude can also be seen as the negative amplitude close to the inner core neighbors zero in the fast rotating case. In a similar fashion, the difference between positive and negative amplitudes of u_ϕ close to the outer boundary is lower in the fast rotating case. This means that the inner region is spun-up and the outer region is instead spun-down for this particular resonance.

The non-rotating case is both qualitatively and quantitatively different as compared to the rotating cases: for u_r , the $m = 2$ mode is still dominant but the number of radial nodes is in-

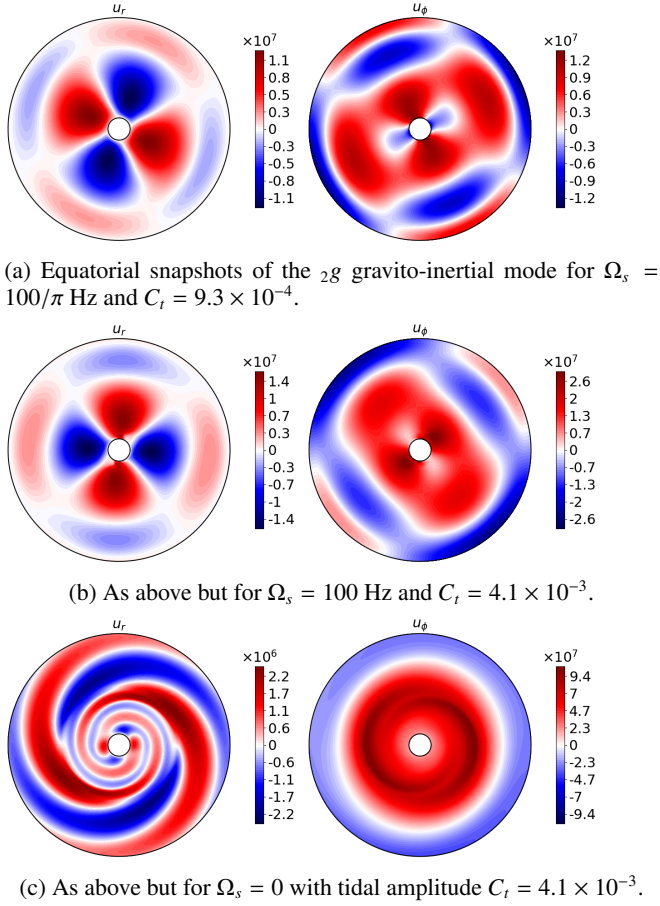


Fig. 15: Velocity flows, u_r (left) and u_ϕ (right), of the gravito-inertial $2g$ mode in the equatorial plane for $\Omega_s = 100/\pi$ Hz, (top), $\Omega_s = 100$ Hz (middle), and $\Omega_s = 0$ with an increased tidal amplitude (bottom).

creased, especially in the inner region, and the amplitude is a factor ~ 5 lower. For u_ϕ , the $m = 0$ mode is dominant with the addition of “spiral arms” that looks like a superposition of $m = 2$ and $m = 1$ modes. The amplitude of u_ϕ is also ~ 4 times stronger compared to the rotating cases. This strong spin-up in the inner region might explain why different radial modes are excited for this non-rotating case. Indeed, the spin-up leads to a rotation rate of $\Omega_{\text{spin-up}} \approx 20$ Hz, which would modify the tidal forcing frequency from $\hat{\omega} = 0.127N$ to $\hat{\omega} \approx 0.038N$. This would lead to the excitation of higher radial-number gravity-modes and could explain the splitting of the domain in two regions, where the excited modes appear more like $3g$ ($1g$) in the inner (outer) region.

We can confirm the overall spin-up in the domain for all three cases by looking at the toroidal velocity u_ϕ in the meridional plane (Figure 16). First, we see that the non-axisymmetric contribution is stronger than the axisymmetric contribution at a lower tidal amplitude as non-linear effects are less important. When modes become more non-linear, the axisymmetric part becomes of the same order as the non-axisymmetric component and even dominates for the non-rotating case with increased amplitude. By increasing rotation, the modes becomes more cylindrical as it can be seen in the $\Omega_s = 100$ Hz case, while they are spherical when $\Omega_s = 100/\pi$ Hz and $\Omega_s = 0$. In the non-rotating case, we also see the same radial geometry observed in the equatorial plane: the gravity $2g$ mode seems to be split into a $3g$ mode in the inner region and $1g$ mode in the outer region. We compute

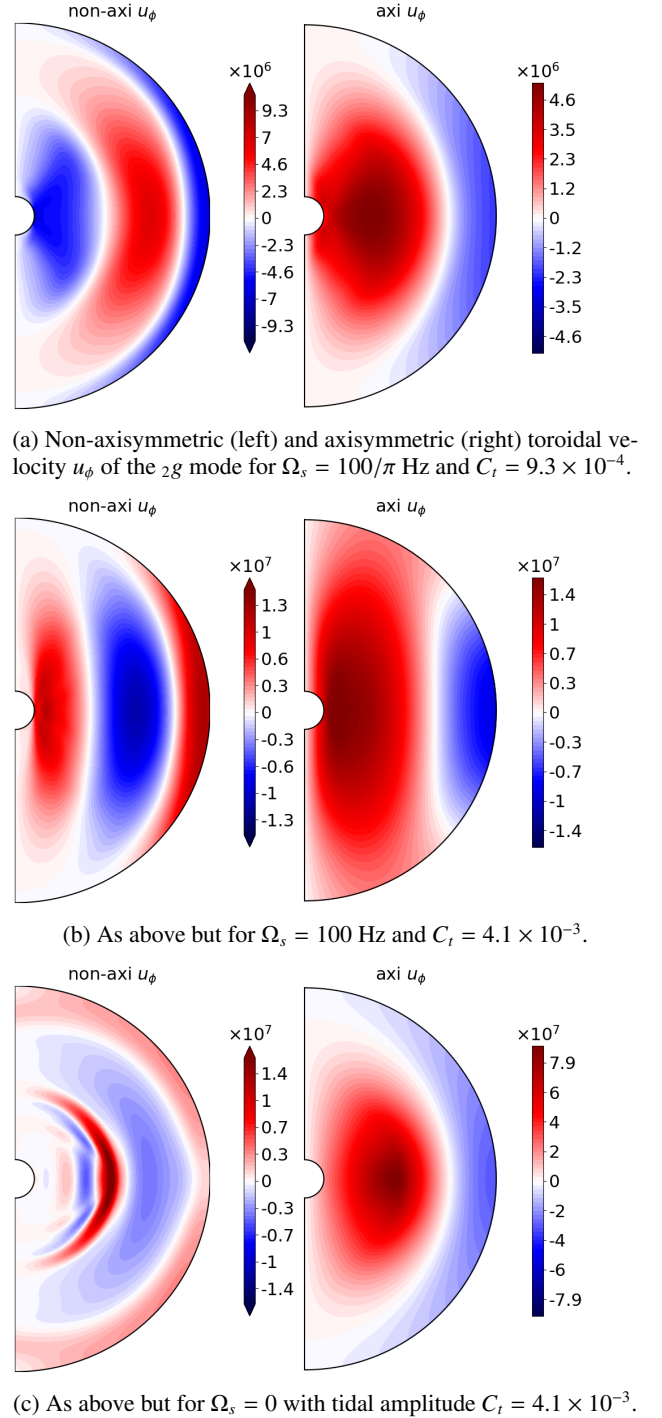


Fig. 16: Velocity flow of the gravito-inertial $2g$ mode in the meridional plane for $\Omega_s = 100/\pi$ Hz, (top), $\Omega_s = 100$ Hz (middle), and $\Omega_s = 0$ with an increased tidal amplitude (bottom).

the vertical angular momentum following

$$L_z = \int_V (r \sin\theta)^2 \Omega \, dV, \quad (34)$$

with $\Omega = u_\phi / (r \sin\theta)$, to estimate the spin up in the inner half of the domain V from $r = 0.1R_o$ to $r = 0.55R_o$. We then estimate the solid body rotation at the end of the simulation $\Omega_{s,end}$ that

would correspond to this angular momentum, viz.

$$\Omega_{s,end} = \frac{L_z}{\int_V (r \sin\theta)^2 dV}. \quad (35)$$

We find that $\Omega_{s,end} \in [21.58\text{Hz}, 1.0476\Omega_s, 1.042\Omega_s]$ for initial values $\Omega_s \in [0, 100/\pi, 100]$ Hz. With stronger non-linear effects (i.e, stronger tidal amplitude and/or reduced rotation), the absolute value of the spin-up is stronger as it goes from $\Omega_{s,end} - \Omega_s = 1.5$ Hz to 21.58Hz.

5.2.2. $1g$ mode

Using the same strategy, we turn our attention to $1g$ modes. The tidal forcing frequencies of the $1g$ mode are $\hat{\omega} \in [0.235N, 0.21775N, 0.13180N]$ for $\Omega_s \in [0, 100/\pi, 100]$ Hz, and the tidal dimensionless amplitudes are $C_t = 1.6 \times 10^{-3}$ and $C_t = 5.3 \times 10^{-3}$ for the two rotating cases. As for the $2g$ mode, we use the same tidal amplitude in the non-rotating case as the more-rapidly rotating case $C_t = 5.3 \times 10^{-3}$ instead of the realistic one $C_t = 1.36 \times 10^{-3}$. Figure 17 shows time evolutions for the different kinetic energies, which for all simulations would be enough to generate a magnetic field stronger than 10^{15} G assuming equipartition. The non-linearities become relevant for both modes after less than 1 s after initialization.

The evolution of the $1g$ modes is quite different from the $2g$ mode as after a first growth, some fast oscillations of the kinetic energy appear. These oscillations may be indicating that the $1g$ mode is subject to parametric instabilities or corotation resonance instabilities. Before looking more into the instabilities, we note that similar results to those obtained for the $2g$ mode are found for the importance of non-linear effects. Indeed, for $\Omega_s = 100/\pi$ Hz, the poloidal kinetic energy dominates and the axisymmetric energy represents again around $\sim 20\%$ of the total kinetic energy. For $\Omega_s = 100$ Hz, the non-linear effects are even stronger as axisymmetric energy represents $\approx 50\%$ of the budget. In addition, the toroidal and poloidal components contribute evenly to the total kinetic energy at the end of the simulation. To understand the impact of rotation and tidal amplitude, we compare this evolution with that of the non-rotating case with the same tidal amplitude. We find a critical difference for $\Omega_s = 0$: the non-linear effects become important sooner in the evolution, and the axisymmetric toroidal kinetic energy becomes dominant after 1 s. The time evolution for the non-rotating case is quite interesting as the first growth is higher than the other cases but it drops quicker, until stabilizing after 4 s. The first decreasing part is due to the evolution of an instability, as we see small oscillations in the poloidal kinetic energy until the $m = 2$ mode grows again and dominates the energy contribution for the second part after 4 s.

To better understand these three simulations, we look at the kinetic energy spectra along degrees ℓ and orders m at the end of the time evolution (Figure 18). The difference with the $2g$ mode is quite clear as there are no patterns between odd and even degrees. This means that equatorial symmetry is broken by an instability. For both rotating cases, the spectrum is continuous, meaning that non-linear effects are strong. This can be seen as well on the order spectrum, where, for the rotating cases, the dominant mode for the poloidal component is not the $m = 2$ mode (of the initial tidally-forced waves) but the $m = 1$ mode. For the toroidal component, there is also a strong $m = 1$ mode but the $m = 0$ mode is dominant. The emergence of this $m = 1$ mode indicates that an instability appears in this simulation. In the cases of fastest rotation and no rotation for which non-linear

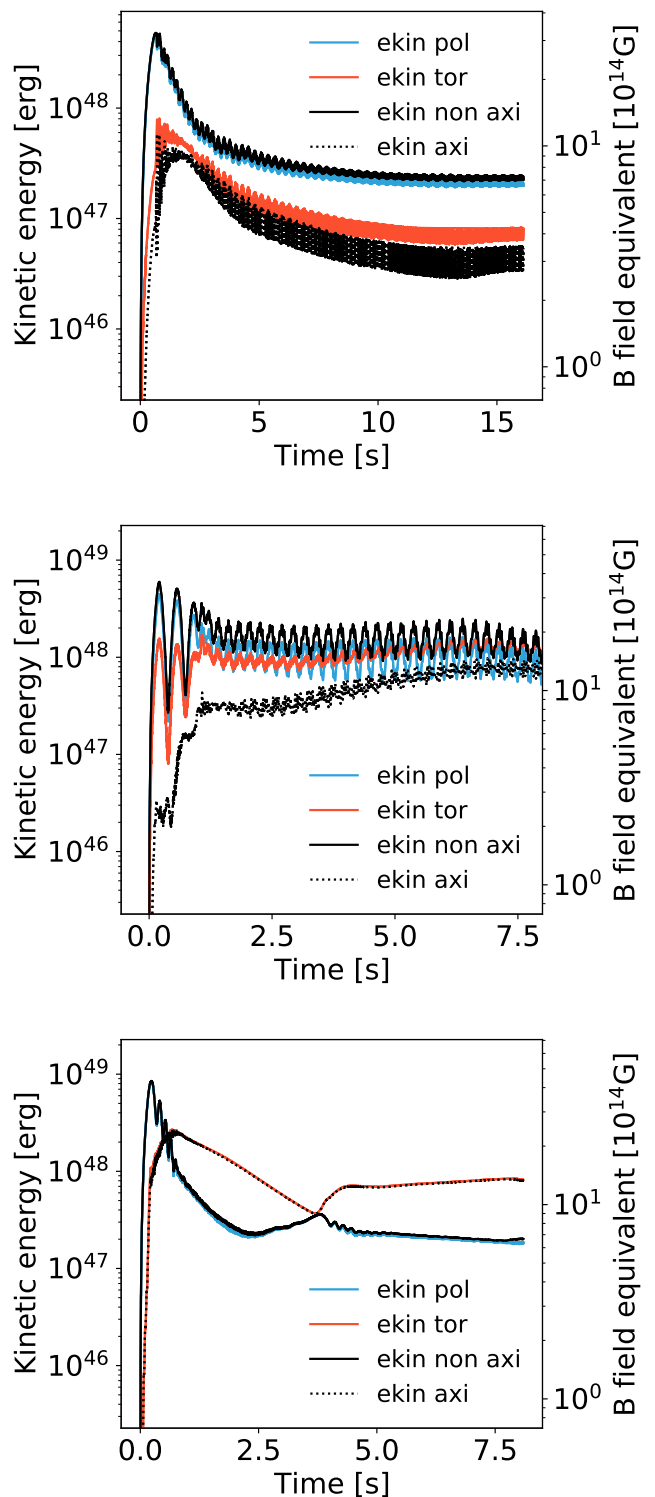
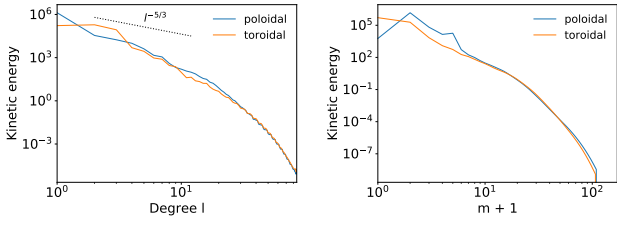
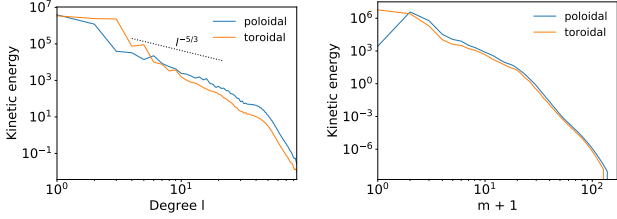


Fig. 17: Time evolution of the kinetic energy for the $1g$ mode for $\Omega_s = 100/\pi$ Hz (top), $\Omega_s = 100$ Hz (middle), and $\Omega_s = 0$ with an increased tidal amplitude $C_t = 5.3 \times 10^{-3}$ (bottom).

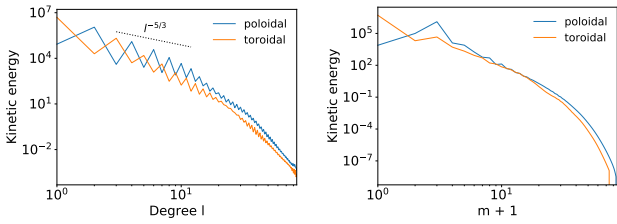
effects are the strongest, the energy cascade from high to small spatial scales approaches a Kolmogorov spectrum, $\propto \ell^{-5/3}$, at moderate spherical harmonics degrees. In the low rotation case [panel (a) in Fig. 18], the spectra are steeper than $\ell^{-5/3}$. The energy cascade towards different parity modes and smaller spa-



(a) Kinetic energy spectra of the $2g$ mode for $\Omega_s = 100/\pi$ Hz and $C_t = 1.36 \times 10^{-3}$.



(b) As above but for $\Omega_s = 100$ Hz and $C_t = 5.3 \times 10^{-3}$.



(c) As above but for $\Omega_s = 0$ with tidal amplitude $C_t = 5.3 \times 10^{-3}$.

Fig. 18: Similar to Fig. 14 but for the $1g$ -mode. The dotted line corresponds to the slope $\ell^{-5/3}$.

tial scales may indicate the onset of wave turbulence, as found in other setup of unstratified hydrodynamical turbulence driven by triadic resonances of inertial waves (see for instance Galtier 2003; Barik et al. 2018, 2024). The stronger tidal amplitude enhances the non-linear effects but, in the non-rotating case, the scaling $\ell^{-5/3}$ is not seen in the kinetic spectra even when the triadic resonance is dominant.

To characterize the instability and the oscillations that appears for the rotating simulations, we perform a Fourier transform of the poloidal scalar potential $W(l, m, r_{FFT})$ at mid-point of the domain $r_{FFT} = 0.55$ for the different main modes for the slower and faster rotating cases and non-rotating case (Figure 19). For both rotating cases, we find that the dominating component is the $(l, m) = (1, 1)$ mode and the oscillations of this mode are divided in two frequencies ω_1 and ω_2 . We call ω_1 the main frequency at $\omega_1 = 63.098$ Hz and $\omega_1 = 58.184$ Hz, for $\Omega_s = 100/\pi$ Hz and $\Omega_s = 100$ Hz, respectively. We also see that the second main mode is the expected $(l, m) = (2, 2)$ modes but some further modes are also excited along with a number of even $\ell + m$ modes (due to symmetry; while odd $\ell + m$ being excited for the toroidal velocity potential), especially for the highest-rotation case where the tidal amplitude and non-linear effects are stronger. The $(l, m) = (2, 2)$ is excited at the tidal forcing frequency $\hat{\omega}$ and the $(l, m) = (4, 4)$ is excited at its superharmonics $2\hat{\omega}$ in the fast rotating case only. The second tallest peak of the $(l, m) = (1, 1)$ mode is at the frequency $\omega_2 = \hat{\omega} - \omega_1$. Therefore, it seems that the $m = 1$ mode is growing at the expense of the main $m = 2$ forcing mode, which would explain why the latter is not dominant anymore (com-

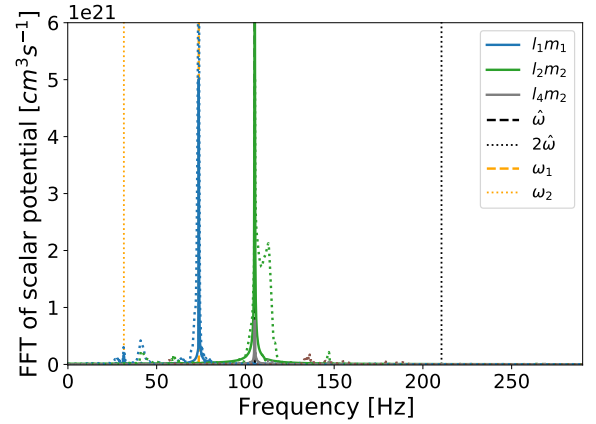
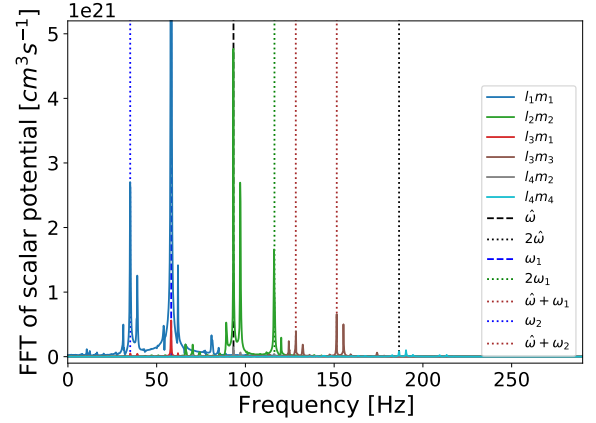
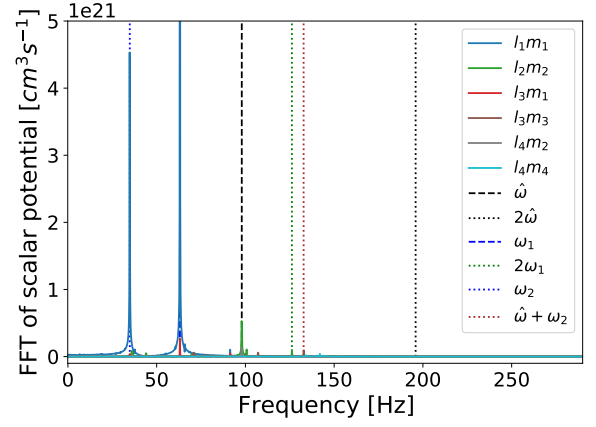
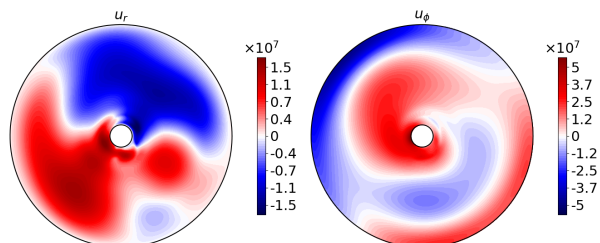


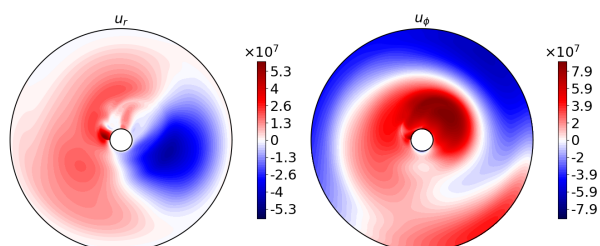
Fig. 19: Fourier transform of the poloidal velocity potential W showing the different main modes for $\Omega_s = 100/\pi$ Hz (top), $\Omega_s = 100$ Hz (middle), and $\Omega_s = 0$ (bottom). We have $\omega_1 \in [63.1, 58.2, 73.7]$ Hz and $\omega_2 = \hat{\omega} - \omega_1$. In the non-rotating case, the FFT in the first phase $t \in [0, 4]$ s is plotted in dotted line, while the second phase $t \in [4, 10]$ s is plotted in solid lines.

pared to simulations without the instability). All these observations provide clear evidence for triadic resonances (theorized and observed for inertial waves in Kerswell 1999; Barik et al. 2018; Astoul & Barker 2022) since all of the excited modes can be recovered by a linear combination of $\hat{\omega}$ and ω_1 and their corresponding degrees and orders. In particular, we recover the modes $(l, m) = (3, 3) = (2, 2) + (1, 1) = (4, 4) - (1, 1)$, with both excited frequencies $\omega_{3,3} \in [\hat{\omega} + \omega_1, 2\hat{\omega} - \omega_1] = \hat{\omega} + \omega_2$.

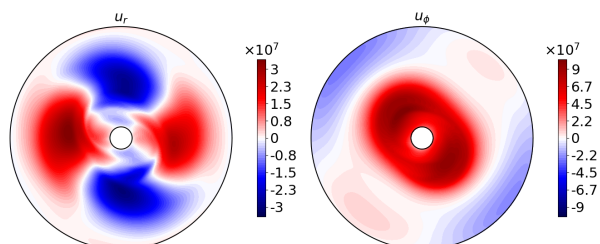
In the fast rotating case, we can see the impact of rotation as main frequencies are split between a slight higher frequency and lower frequency. The new peaks appearing with fast rotation can also be recovered by linear combination of the $\hat{\omega}$ and ω_1 and their corresponding split frequencies. This may be a sign that the rotation is increased in some part of the domain and decreased in the other part, which would shift, respectively, the frequency to lower frequencies or higher frequencies.



(a) Equatorial snapshot of velocities associated with the $1g$ gravito-inertial mode for $\Omega_s = 100/\pi$ Hz and $C_t = 1.36 \times 10^{-3}$.



(b) As above but for $\Omega_s = 100$ Hz and $C_t = 5.3 \times 10^{-3}$.



(c) As above but for $\Omega_s = 0$ with tidal amplitude $C_t = 5.3 \times 10^{-3}$.

Fig. 20: Similar to Fig. 15 but for $1g$ modes.

To spatially visualize the triadic resonances, we first look at snapshots of the radial u_r and toroidal u_ϕ velocity in the equatorial plane (Figure 20). As expected from previous diagnostics, the $m = 1$ mode is clearly dominant for both rotating cases. The velocity components u_r and u_ϕ are overall stronger in the case with higher rotation. The radial structure in the two cases is similar with the half-wavelength mode dominating for u_r and full-wavelength one for u_ϕ , as expected for the $1g$ mode. Some small scale structure with strong amplitude is present close to the inner boundary. One could think that the inner boundary, and the development of a Stewartson layer at the inner tangent cylinder (Stewartson 1966; Barik et al. 2018, 2024), is at the origin of this parametric instability, but we also observe a similar growing $\ell = m = 1$ mode in a test simulation with a full sphere (not shown here). The increase in non-linear effects with the fast rotation can also be seen in u_ϕ as the $m = 1$ mode is less important compared to the $m = 0$ mode. In this case, the zonal flow looks more like the one for the $2g$ mode, where the inner region is spun-up and the outer region is spun-down.

In the non-rotating case, we find similar results to the previous $2g$ mode where instead $m = 2$ ($m = 0$) is dominant for

the radial (toroidal) velocity. In terms of amplitude, the velocity components of the $1g$ mode seem to have a similar amplitude as the faster rotating case (comparing panels (b) and (c) of Fig. 17), though it is difficult to compare directly as one is due to triadic resonances, while, at the end of the non-rotating simulation, the mode is a more typical tidally-excited $\ell = m = 2$ mode for the poloidal component (panel (c) in Fig. 20). This is confirmed by the comparison of the fast Fourier transform (FFT) of the non-rotating case before 4 s (dotted lines) and after 4 s (solid lines); see the bottom panel of Figure 19). In the non-rotating case, there seems to be a weaker mode close to the inner region and a stronger mode in the center of the domain. This may be due once again to the strong spin-up that we see in the inner region via u_ϕ in the panels (c) in Figures 20 and 21.

We can confirm spin-up in the inner region for all three cases by looking at the axisymmetric toroidal velocity u_ϕ in the meridional plane (right panels of Figure 21). First, we see similar effects of rotation and increased tidal amplitude than for the $2g$ mode: when modes become more non-linear (increased tidal amplitude/reduced rotation), the axisymmetric component becomes stronger compared to the non-axisymmetric component and clearly dominates for the non-rotating case with increased amplitude. The impact of rotation is also clearly seen as the flow with $\Omega_s = 100$ Hz is more cylindrical than the other cases, whereas the spherical geometry of gravity dominates in the two other cases. The geometry for the non-axisymmetric components is different as there is only one radial wavelength and there are more structures close to the inner core. The axisymmetric component also seems to be shifted towards the interior compared to the $2g$ mode (Figure 16). By comparing the right panels of Figure 16 and Figure 21, we see that the axisymmetric toroidal velocity is stronger for the $1g$ mode in the rotating cases, which may be due to the increased tidal amplitude and also that the $1g$ mode resonance is stronger even for a similar tidal amplitude (see Section 2.2.2).

To confirm that the inner spin-up is stronger for this simulation, we estimate the spin up in the first half of the shell as in Eq. (35). We find that $\Omega_{s,end} \in [17.3 \text{ Hz}, 1.1\Omega_s, 1.18\Omega_s]$ for an initial $\Omega_s \in [0, 100/\pi, 100]$ Hz. This is consistent with the fact that the axisymmetric azimuthal velocities are stronger for the $1g$ mode in rotating cases.

Implications for dynamo activity and gravitational waves

We find that the kinetic energy of the tidally excited flow would be enough to generate a magnetic field of $> 10^{14}$ G for the $2g$ mode and $> 10^{15}$ G for the $1g$ mode. However, the bulk of this energy will likely be localized to small scales and it is unclear if the corresponding dipole growth would be enough to explain precursor luminosities. Under the assumption of an incompressible fluid and the smooth BV frequency shown in Fig. 11, the modes are localized closer to the core than to the crust and would most likely generate the magnetic field there. However, from linear calculations with a realistic NS profile with the APR4 EOS, the mode velocity is faster in the crust, so we can expect (in principle) to have the differential rotation in the crust, where it would amplify the magnetic field that is most relevant for electromagnetic observables. If we assume that the strength of the dipole is 5% of the total magnetic field, as found in simulations of the magnetorotational instabilities (Reboul-Salze et al. 2021, 2022), it may be enough to explain the luminosity of precursors (Suvorov et al. 2024a). This needs to be further studied in simulations with magnetic transport included and compared with a

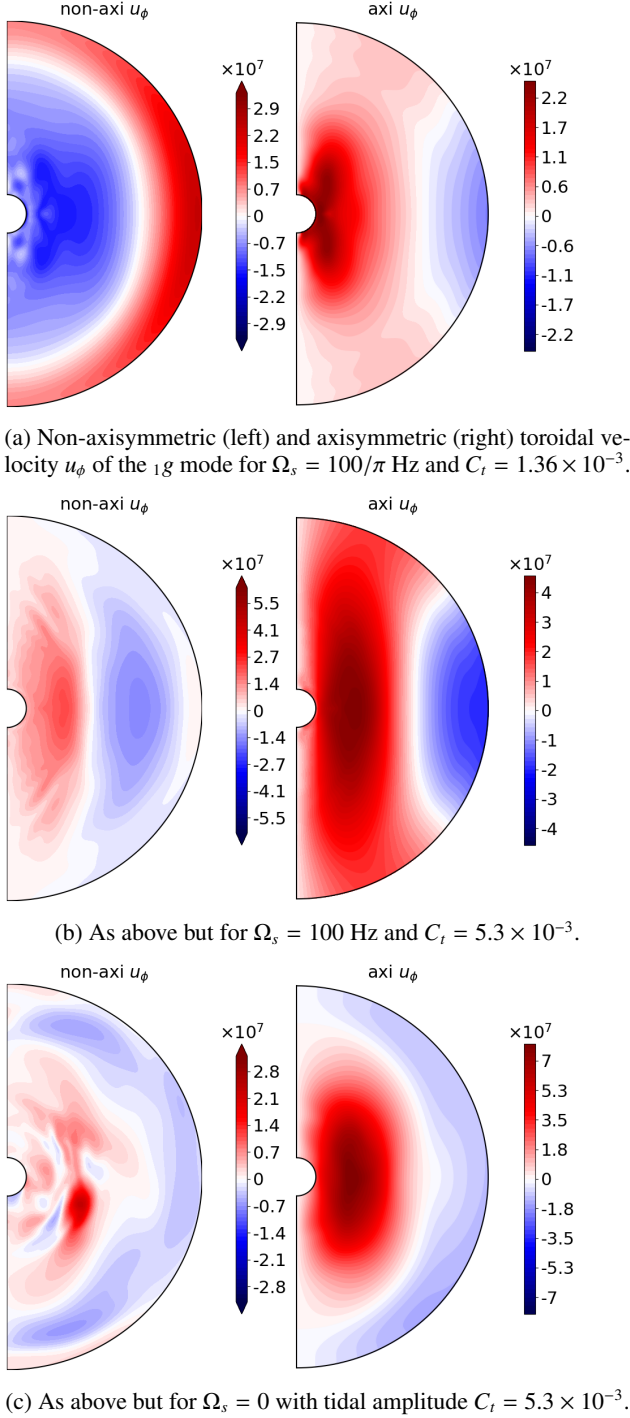


Fig. 21: Similar to Fig. 16 but for the $1g$ mode.

more-realistic interior, which is out of the scope of this paper. Still, the results are promising.

We also find that the star, for $2g$ and $1g$ modes and for all rotation rates, would get spin-up by the resonance. This implies that we can expect the tidal forcing frequency $\hat{\omega} = 2(\Omega_o - \Omega_s)$ to remain in resonance window longer as the orbital frequency Ω_o evolves due to the emission of GWs. This depends on the size of the window but roughly lies in the range $0.99\omega_{\text{resonant}} \leq \hat{\omega} \leq 1.01\omega_{\text{resonant}}$, so that a spin-up of 10% would increase the resonant window timescale by a factor ~ 5 .

6. Discussions

6.1. Consequences for BH-NS mergers

The calculations done in this study are practically independent of the particulars regarding the secondary of mass M_2 . We could therefore extrapolate our results to cases relevant for a black-hole with $M_2 > M_1$. This means that the tidal amplitude parameter $\epsilon = \frac{M_2}{M_1} \left(\frac{R_o}{a}\right)^3$ would increase for a given semi-major axis a . This may lead to stronger tidal amplitudes; in particular, for a given orbital frequency Ω_o corresponding to a resonant frequency, the tidal amplitude parameter ϵ can be written as $\epsilon = \frac{M_2}{M_1 + M_2} \left(\frac{\Omega_o}{\omega_d}\right)^2$ by using $a^3 = \frac{G(M_1 + M_2)}{\Omega_o^2}$ and $R_o^3 = \frac{GM_1}{\omega_d^2}$, which would increase by a maximum factor ~ 2 . Stronger non-linear effects are therefore expected, provided the resonance occurs, most likely without changing qualitatively the results of this study.

6.2. Interior structure

Comparison between results from Secs. 4 and 5 shows the importance of the NS interior model. Indeed, the BV frequency in section 5 is higher by a factor $\approx 2 - 5$ from the inner to the outer boundaries. This increase in the BV frequency lead to stronger non-linear effects. As the BV frequency is strongly dependent on the internal microphysics, a change in the NS model could impact the conclusions of this study. Additionally, the tidal amplitude parameter is dependent on the NS radius R_o and an increase of 20% in this quantity for a different EOS at a fixed mass would lead to an increase of ≈ 1.7 in the amplitude of a given mode, which may then change the non-linear saturation (see also Suvorov et al. 2024b). The density profile also changes with the EOS, which would further impact on the mode eigenfunctions. Density profiles can be taken into account with an anelastic model, the development of which is left to future studies owing to numerical challenges: the density gradient have to be taken into account in the computation of the equilibrium tides. This would be especially important in studying the resonant modes in the crust, where proposed late-stage amplifications of near-surface magnetic fields have been invoked to explain the luminosity of GRB precursors as the Ohmic decay timescale is expected to be much shorter than the orbital lifetime (e.g. Pons & Viganò 2019).

6.3. Formulation issues

As with most numerical studies of astrophysical phenomena, some limitations are inevitable as physical time- and length-scales typically span many orders of magnitude in such systems. Indeed, the formulation presented in this article has a few limitations, which we highlight here and in the sections below for completeness.

(i) The formulation cannot reproduce f -mode resonances or g -mode resonances too close to the f -mode frequency as this mode is ‘hard coded’ in the static tide (the Love number in the equilibrium velocity). Moreover, a fixed surface is a poor approximation for f -mode oscillations (Pontin et al. 2023). (ii) In the non-resonant regime, the formulation cannot reproduce results with a free surface. This can be corrected by changing the stress-free boundary conditions to match the free surface case. However, its implementation with the scalar potentials in the non-linear code can be difficult or may lead to unexpected effects and the study of the regime, away from the BV frequency, is left to further studies. (iii) The use of a spherical shell leads

to the neglecting of non-linear interactions between the equilibrium and dynamical tides. It can be justified by some considerations (see [Astoul & Barker 2022](#)) but when the resonant modes occupy the largest scales, these non-linear interactions might become relevant.

6.4. Cowling approximation

A simplifying hypothesis employed throughout is the Cowling approximation, the neglect of equilibrium and dynamical perturbations to the background gravitational potential $\nabla\Phi_g = \mathbf{g}$. These effects could have a strong impact on the amplitude of the modes however; the linear study of [Xu & Lai \(2017\)](#) found a reduction down to 20% of the initial amplitude in cases without perturbations to the self-gravity potential. Nonetheless, it is unknown how the dynamical perturbations to self-gravity Φ'_g in our setup, where we assume a constant density, would impact the modes and their non-linear saturation. In addition, neglecting the equilibrium perturbations to self-gravity Φ_g^e removes a term $\propto (1+k_2)$ in the amplitude of the equilibrium tide, where k_2 is the Love number associated with the $\ell = 2$ tide. For NSs, realistic calculations of Love numbers give $k_2 \gtrsim 0.1$ ([Flanagan & Hinderer 2008](#); [Hinderer 2008](#); [Hinderer et al. 2010](#)), meaning we underestimate the amplitude by $\gtrsim 10\%$. Overall, we seem to be neglecting both positive and negative effects of the self-gravity and the impact of this assumption needs to be further studied as it could be exacerbated to some degree for a realistic stellar density profile.

6.5. Dissipation processes

The simulations presented in this work have been carried out with unrealistic viscosities and thermal/compositional diffusivities that could change the results. For example, in a NS, the microphysical viscosities are estimated to be at least 10 orders of magnitude lower than that used here. For the thermal/composition diffusivities, the value depends highly on the NS model and evolutionary pathway (e.g. whether there was a history of recycling; see [Suvorov et al. 2024b](#)). In linear studies, such as [Pontin et al. \(2023, 2024\)](#), it has been found that decreasing the viscosity/thermal diffusivity by ~ 2 orders of magnitude leads to a comparable increase to the total (frequency-dependent) tidal dissipation and mode kinetic energy. On a positive note, this suggests that the mode amplitudes found in this study can be seen as lower limits and may be larger in astrophysical circumstances. This also means that non-linear effects are more relevant, especially with respect to how saturation depends on damping processes. It is for this reason that we chose to study the non-rotating case with an increased tidal frequency. However, triadic resonances, corotation resonances, or other secondary instabilities (like shear-flow instabilities) may lead to a different saturation mechanism that is largely insensitive to the viscosity and thermal diffusivity below some critical values. Studying the impact of viscosity and thermal diffusivity is required to understand the non-linear saturation and to explore a wider range of parameters; this will be the subject of future work.

Moreover, the resonant peaks (see, e.g., [Fig. 1](#)) may also become narrower and the relevant resonant window itself could become smaller. A study that takes into account the evolution of the tidal forcing frequency and tidal amplitude due to the emission of GWs would be required to see whether the modes are able to draw enough energy from the time-varying orbit and reach a similar amplitude as the modes presented in this study.

7. Conclusions and perspectives

In this article, a new formulation, building on that of [Astoul & Barker \(2022, 2023\)](#) but applied here to a stably- instead of neutrally-stratified region, was derived in order to simulate the non-linear saturation of gravito-inertial modes in a self-consistent manner that separates equilibrium and dynamical tides. To ensure consistency with previous formulations that do not distinguish between dynamical/equilibrium tides, we first tested the linear limit of this scheme and found excellent agreement with previous studies for both pure and gravito-inertial modes provided the tidal forcing frequency is not so high so as to be close to the f- or acoustic-mode frequencies ([Sec. 3](#)), where nonlinear effects may be important in any case ([Kuan et al. 2024](#)).

The non-linear code was benchmarked against the linear results in [Sec. 3](#) with a uniform entropy/composition gradient, finding again quantitative agreement in the expected regimes of validity. With a homogeneous BV frequency of $N = 0.045\omega_d$ and a dimensionless tidal amplitude of $C_t \sim 10^{-3}$, such a comparison demonstrated the impact of non-linear effects for several modes in the form of a generated, axisymmetric kinetic energy representing $\gtrsim 5\%$ of the total kinetic energy. In particular, we found in [Sec. 4](#) that the strongest resonant modes are indeed able to generate an axisymmetric kinetic energy representing of order 10% of the total kinetic energy. This axisymmetric component is dominated by the toroidal velocity u_ϕ , which is optimistic from the perspective of enticing premerger dynamo activity and the generation of magnetic fields, as first suggested by [Suvorov et al. \(2024b\)](#).

Although the formalism is general, it has been primarily applied in the context of neutron-star binaries in this work; astrophysical applications for gravito-inertial modes were considered in [Sec. 5](#). A BV profile based on TOV calculations with the APR4+DH EOS, smoothed out in the crust, was considered in an effort to consider realistic profiles even though the formalism here is strictly Newtonian; such hybrid schemes are common in the literature, especially because a fully-relativistic treatment of tides is difficult (see [Suvorov et al. 2024b](#), for a discussion). Comparisons with the GR linear calculations demonstrate quantitative agreement for pure g-modes in the stellar core but not in the crust (see [Fig. 12](#)). This is primarily due to the impact of the radially-varying density profile and compositional discontinuities in the crust that we neglect in this study via the Boussinesq approximation. The linear code was then used to compute the resonant frequencies to study the non-linear saturation of the $1g$ and $2g$ modes. We found that with a stronger BV frequency compared to [Sec. 4](#), non-linear effects dominate even more in determining the saturation of the modes. Remarkably, the axisymmetric kinetic energy can constitute up to 95% of the total mode energy. Overall, we argue that if the kinetic energy was efficiently converted into magnetic energy a magnetic field of $10^{14} - 10^{15}$ G could be generated. If this occurs via the magnetorotational instability, appealing to previous studies that quantified multipolar energy distributions ([Reboul-Salze et al. 2021, 2022](#)) suggests the anticipated strength of the dipole component would be between $5 \times 10^{12} - 5 \times 10^{13}$ G. This would be enough to explain the luminosity of (at least most) precursors (e.g. [Tsang et al. 2012](#); [Xiao et al. 2024](#)).

We also find that the NS should get spun-up by resonances as u_ϕ is non-negligible (e.g. [Fig. 16](#)). The rotation rate in the inner half of the domain may be increased by up to $\sim 10\%$ for already-rotating cases and up to ~ 20 Hz in the non-rotating case. Such an increase would lead to the tidal forcing frequency

$\hat{\omega} = 2(\Omega_o - \Omega_s)$ remaining in the resonance window for longer as the orbital frequency Ω_o sweeps up due to the emission of GWs. Linear studies of gravito-inertial modes in NSs may therefore underestimate the amplitude of these modes as this lengthening, and hence the duration of energy transfer, has not been considered. Stronger saturation should therefore be studied in more detail as it could lead to a greater degree of dephasing and makes a more optimistic case for the detectability of dynamical tides with next-generation GW interferometers (Ho & Andersson 2023).

Acknowledgements

Linear simulations were run on the Yamazaki cluster at the Max-Planck Institute for Gravitational Physics, Potsdam. Non-linear simulations were run on the Sakura cluster at the Max Planck Computing and Data Facility (MPCDF) in Garching, Germany. AGS is grateful for support provided by the Conselleria d'Educació, Cultura, Universitats i Ocupació de la Generalitat Valenciana through Prometeu Project CIPROM/2022/13. AA has been funded by a Leverhulme Trust Early Career Fellowship (ECF-2022-362). The authors thank A. Barker for helpful discussions about the treatment of tides, and more specifically the validity of different dynamical/equilibrium tide decompositions.

References

- Aerts, C. & Tkachenko, A. 2024, *A&A*, 692, R1
- Akmal, A., Pandharipande, V. R., & Ravenhall, D. G. 1998, *Phys. Rev. C*, 58, 1804
- Alexander, M. E. 1987, *MNRAS*, 227, 843
- Andersson, N. & Pnigouras, P. 2020, *Phys. Rev. D*, 101, 083001
- Astoul, A. & Barker, A. J. 2022, *MNRAS*, 516, 2913
- Astoul, A. & Barker, A. J. 2023, *ApJ*, 955, L23
- Astoul, A. & Barker, A. J. 2025, arXiv e-prints, arXiv:2501.08722
- Baiko, D. A. 2024, *MNRAS*, 528, 408
- Baiko, D. A. & Chugunov, A. I. 2018, *MNRAS*, 480, 5511
- Balbus, S. A. & Hawley, J. F. 1998, *Reviews of Modern Physics*, 70, 1
- Barik, A., Triana, S. A., Hoff, M., & Wicht, J. 2018, *Journal of Fluid Mechanics*, 843, 211
- Barik, A., Triana, S. A., Hoff, M., & Wicht, J. 2024, *Journal of Fluid Mechanics*, 1001, A1
- Barker, A. J. 2011, *MNRAS*, 414, 1365
- Barker, A. J. 2016, *MNRAS*, 459, 939
- Barker, A. J. 2022, *ApJ*, 927, L36
- Barker, A. J. & Ogilvie, G. I. 2010, *MNRAS*, 404, 1849
- Bolmont, E. & Mathis, S. 2016, *Celestial Mechanics and Dynamical Astronomy*, 126, 275
- Burns, K. J., Vasil, G. M., Oishi, J. S., Lecoanet, D., & Brown, B. P. 2020, *Physical Review Research*, 2, 023068
- Christensen, U. & Wicht, J. 2015, in *Treatise on Geophysics (Second Edition)*, second edition edn., ed. G. Schubert (Oxford: Elsevier), 245 – 277
- Ciolfi, R. 2020, *General Relativity and Gravitation*, 52, 59
- Coppin, P., de Vries, K. D., & van Eijndhoven, N. 2020, *Phys. Rev. D*, 102, 103014
- Counselman, III, C. C. 1973, *ApJ*, 180, 307
- Couston, L.-A., Lecoanet, D., Favier, B., & Le Bars, M. 2018, *Phys. Rev. Lett.*, 120, 244505
- Damour, T. & Nagar, A. 2009, *Phys. Rev. D*, 80, 084035
- Dhouib, H., Baruteau, C., Mathis, S., et al. 2024, *A&A*, 682, A85
- Dintrans, B. & Rieutord, M. 2000, *A&A*, 354, 86
- Dintrans, B., Rieutord, M., & Valdetarro, L. 1999, *Journal of Fluid Mechanics*, 398, 271
- Douchin, F. & Haensel, P. 2001, *A&A*, 380, 151
- Duchêne, G. & Kraus, A. 2013, *ARA&A*, 51, 269
- El-Badry, K. 2024, *New A Rev.*, 98, 101694
- Favier, B., Barker, A. J., Baruteau, C., & Ogilvie, G. I. 2014, *MNRAS*, 439, 845
- Flanagan, É. É. & Hinderer, T. 2008, *Phys. Rev. D*, 77, 021502
- Fuller, J., Guillot, T., Mathis, S., & Murray, C. 2024, *Space Sci. Rev.*, 220, 22
- Galtier, S. 2003, *Phys. Rev. E*, 68, 015301
- Gastine, T. & Wicht, J. 2012, *Icarus*, 219, 428
- Gilman, P. A. & Glatzmaier, G. A. 1981, *ApJS*, 45, 335
- Goldreich, P. & Nicholson, P. D. 1989, *ApJ*, 342, 1079
- Guo, Z., Ogilvie, G. I., & Barker, A. J. 2023, *MNRAS*, 521, 1353
- Hegade K. R., A., Ripley, J. L., & Yunes, N. 2024, *Phys. Rev. D*, 109, 104064
- Hinderer, T. 2008, *ApJ*, 677, 1216
- Hinderer, T., Lackey, B. D., Lang, R. N., & Read, J. S. 2010, *Phys. Rev. D*, 81, 123016
- Hinderer, T., Taracchini, A., Foucart, F., et al. 2016, *Phys. Rev. Lett.*, 116, 181101
- Ho, W. C. G. & Andersson, N. 2023, *Phys. Rev. D*, 108, 043003
- Jackson, B., Greenberg, R., & Barnes, R. 2008, *ApJ*, 678, 1396
- Ji, S., Fuller, J., & Lecoanet, D. 2023, *MNRAS*, 521, 5372
- Kerswell, R. R. 1999, *Journal of Fluid Mechanics*, 382, 283
- Kokkotas, K. D. & Schafer, G. 1995, *MNRAS*, 275, 301
- Kuan, H.-J., Kiuchi, K., & Shibata, M. 2024, arXiv e-prints, arXiv:2411.16850
- Kuan, H.-J., Suvorov, A. G., & Kokkotas, K. D. 2021a, *MNRAS*, 506, 2985
- Kuan, H.-J., Suvorov, A. G., & Kokkotas, K. D. 2021b, *MNRAS*, 508, 1732
- Kuan, H.-J., Suvorov, A. G., & Kokkotas, K. D. 2023, *A&A*, 676, A59
- Kwon, K. J., Yu, H., & Venumadhav, T. 2024, arXiv e-prints, arXiv:2410.03831
- Kwon, K. J., Yu, H., & Venumadhav, T. 2025, arXiv e-prints, arXiv:2503.11837
- Lai, D. & Wu, Y. 2006, *Phys. Rev. D*, 74, 024007
- Lazovik, Y. A., Barker, A. J., de Vries, N. B., & Astoul, A. 2024, *MNRAS*, 527, 8245
- Lecoanet, D., Vasil, G. M., Fuller, J., Cantiello, M., & Burns, K. J. 2017, *MNRAS*, 466, 2181
- Lin, Y. & Ogilvie, G. I. 2018, *MNRAS*, 474, 1644
- Mathis, S. 2009, *A&A*, 506, 811
- Ogilvie, G. I. 2009, *MNRAS*, 396, 794
- Ogilvie, G. I. 2013, *MNRAS*, 429, 613
- Ogilvie, G. I. 2014, *ARA&A*, 52, 171
- Ogilvie, G. I. & Lin, D. N. C. 2004, *ApJ*, 610, 477
- Passamonti, A., Andersson, N., & Pnigouras, P. 2021, *MNRAS*, 504, 1273
- Peters, P. C. 1964, *Physical Review*, 136, 1224
- Pnigouras, P. & Kokkotas, K. D. 2015, *Phys. Rev. D*, 92, 084018
- Pons, J. A. & Viganò, D. 2019, *Living Reviews in Computational Astrophysics*, 5, 3
- Pontin, C. M., Barker, A. J., & Hollerbach, R. 2023, *ApJ*, 950, 176
- Pontin, C. M., Barker, A. J., & Hollerbach, R. 2024, *ApJ*, 960, 32
- Press, W. H. & Teukolsky, S. A. 1977, *ApJ*, 213, 183
- Reboul-Salze, A., Guilet, J., Raynaud, R., & Bugli, M. 2021, *A&A*, 645, A109
- Reboul-Salze, A., Guilet, J., Raynaud, R., & Bugli, M. 2022, *A&A*, 667, A94
- Rieutord, M. 2009, in *The Rotation of Sun and Stars*, Vol. 765, 101–121
- Schaeffer, N. 2013, *Geochem. Geophys. Geosyst.*, 14, 751
- Semin, B., Facchini, G., Pétrélis, F., & Fauve, S. 2016, *Physics of Fluids*, 28, 096601
- Spiegel, E. A. & Veronis, G. 1960, *ApJ*, 131, 442
- Stewartson, K. 1966, *Journal of Fluid Mechanics*, 26, 131
- Suvorov, A. G. & Kokkotas, K. D. 2020, *Phys. Rev. D*, 101, 083002
- Suvorov, A. G., Kuan, H. J., & Kokkotas, K. D. 2022, *A&A*, 664, A177
- Suvorov, A. G., Kuan, H.-J., & Kokkotas, K. D. 2024a, *Universe*, 10, 441
- Suvorov, A. G., Kuan, H.-J., Reboul-Salze, A., & Kokkotas, K. D. 2024b, *Phys. Rev. D*, 109, 103023
- Taniguchi, K. & Shibata, M. 2010, *ApJS*, 188, 187
- Thompson, C. & Duncan, R. C. 1993, *ApJ*, 408, 194
- Tilgner, A. & Busse, F. H. 1997, *J. Fluid Mech.*, 332, 359
- Tsang, D., Read, J. S., Hinderer, T., Piro, A. L., & Bondarescu, R. 2012, *Phys. Rev. Lett.*, 108, 011102
- Wang, J.-S., Peng, Z.-K., Zou, J.-H., Zhang, B.-B., & Zhang, B. 2020, *ApJ*, 902, L42
- Weinberg, N. N., Arras, P., & Burkhart, J. 2013, *ApJ*, 769, 121
- Wicht, J. 2002, *Phys. Earth Planet. Inter.*, 132, 281
- Xiao, S., Zhang, Y.-Q., Zhu, Z.-P., et al. 2024, *ApJ*, 970, 6
- Xu, W. & Lai, D. 2017, *Physical Review D*, 96, 083005
- Yu, H., Arras, P., & Weinberg, N. N. 2024, *Phys. Rev. D*, 110, 024039
- Zahn, J. P. 1966, *Annales d'Astrophysique*, 29, 489
- Zahn, J.-P. 2013, in *Lecture Notes in Physics*, Berlin Springer Verlag, ed. J. Souchay, S. Mathis, & T. Tokieda, Vol. 861, 301
- Zhou, Y. & Zhang, F. 2017, *ApJ*, 849, 114